Chapter 3

Turbulence transport

3.1 Introduction

Over the last few decades, a variety of models have been proposed to describe the spatial evolution of quantities pertaining to the energy and inertial ranges of the power spectra of turbulent magnetic fluctuations in the solar wind [see, *e.g.*, *Zhou and Matthaeus*, 1990; *Tu and Marsch*, 1993; *Oughton and Matthaeus*, 1995; *Zank et al.*, 1996; *Matthaeus et al.*, 1999a; *Smith et al.*, 2001; *Isenberg et al.*, 2003; *Matthaeus et al.*, 2004; *Breech et al.*, 2005; *Isenberg*, 2005; *Oughton et al.*, 2006; *Smith et al.*, 2006b; *Yokoi and Hamba*, 2007; *Breech et al.*, 2008; *Oughton et al.*, 2011; *Zank et al.*, 2012; *Usmanov et al.*, 2012]. Direct applications of such theories to the study of cosmic ray modulation, however, have been relatively few [e.g., *Parhi et al.*, 2003; *Minnie et al.*, 2003, 2005; *Burger and Visser*, 2010; *Pei et al.*, 2010a] and limited to single component models such as that of *Breech et al.* [2008], as opposed to two component turbulence transport models as proposed by, *e.g.*, *Tu and Marsch* [1993], *Oughton et al.* [2006] and *Oughton et al.* [2011]. The present study aims to implement the two-component turbulence transport model of *Oughton et al.* [2011] directly in the study of the heliospheric cosmic-ray diffusion tensor and general modulation. The present chapter serves to introduce the abovementioned model, and present a set of solutions in as close agreement as possible with various turbulence observations throughout the heliosphere discussed in the previous chapter, as well as to investigate the sensitivity of the model to the choice of heliospheric magnetic field model.

3.2 The *Oughton et al.* [2011] model

The *Oughton et al.* [2011] model was chosen for several reasons. Firstly, the two-component approach allows for a more self-consistent treatment of the spatial variation of modelled anisotropic spectra. Using a single component model like that of, *e.g.*, *Breech et al.* [2008], which only describes the spatial variation of quasi-2D quantities, one would have to make relatively *ad hoc* assumptions as to the behaviour of wavelike, or slab quantities. The quasi-2D and wavelike turbulence quantities can also in fair approximation be treated as 2D and slab quantities [*S.*

Oughton, *private communication*, 2011], thereby facilitating their use as inputs for extant cosmic-ray scattering theories [see, *e.g.*, *Shalchi*, 2009]. Secondly, the two-component approach allows for the assignation of energy due to turbulent driving processes to the appropriate component. The energy generated by the formation of pickup ions, previously assigned to the quasi-2D component in the models of *e.g. Zank et al.* [1996]; *Smith et al.* [2001]; *Smith et al.* [2006b]; *Breech et al.* [2008], can now be assigned more properly to the wavelike component [see, *e.g.*, *Hunana and Zank*, 2010; *Oughton et al.*, 2011; *Zank et al.*, 2012]. Lastly, the relative ease with which the equations of the *Oughton et al.* [2011] model can be solved numerically greatly facilitate its application to the study of global cosmic-ray modulation. Note, though, that this model only yields the radial evolution of turbulence quantities at a particular colatitude, and that no latitudinal turbulence transport effects are considered.

A thorough derivation of the two-component model is, however, beyond the scope of this study, and the interested reader is invited to consult *Breech* [2008], *Breech et al.* [2008], and *Oughton et al.* [2011] for greater clarity as to this matter. However, a few words as to its background, and the assumptions made in its derivation, would be useful here. The MHD equations for a compressible, single fluid plasma are the point of departure for many turbulence transport models [see, *e.g.*, *Zhou and Matthaeus*, 1990; *Minnie*, 2006; *Breech*, 2008; *Breech et al.*, 2008]. In the *Oughton et al.* [2011] model, as with its *Breech et al.* [2008] predecessor, the large scale solar wind velocity and magnetic fields are decomposed into a fluctuating component, and a steady, uniform component (see Section 2.1), and the MHD equations are written in terms of the *Elsässer* [1950] variable $\mathbf{z}^{\pm}$, given by

$$\mathbf{z}^{\pm} = \mathbf{v} \pm \frac{\mathbf{b}}{\sqrt{4\pi\rho}}, \tag{3.1}$$

with $\mathbf{v}$ the fluctuating component of the solar wind speed and ρ the proton mass density. Then the scale separated MHD equations can be written as [*Breech et al.*, 2008]

$$\begin{aligned} \frac{\partial \mathbf{z}^{\pm}}{\partial t} & +(\mathbf{V}_{sw} \mp \mathbf{V}_A)\cdot\nabla\mathbf{z}^{\pm} + \frac{1}{2}\nabla\cdot(\mathbf{V}_{sw}/2 \pm \mathbf{V}_A)\mathbf{z}^{\pm} \\ + & \quad \mathbf{z}^{\mp}\cdot\left[\nabla\mathbf{V}_{sw} \pm \frac{\nabla\mathbf{B}_o}{\sqrt{4\pi\rho}} - \frac{\mathbf{I}}{2}\nabla\cdot(\mathbf{V}_{sw}/2 \pm \mathbf{V}_A)\right] \\ = & \quad \mathbf{NL}^{\pm} + \mathbf{S}^{\pm}, \end{aligned} \tag{3.2}$$

where $\mathbf{I}$ denotes the identity matrix, $\mathbf{NL}^{\pm}$ models local nonlinear turbulent effects, and $\mathbf{S}^{\pm}$ any sources. Equation 3.2 is highly nonlinear, and many assumptions are needed to extract a tractable model from it. The *Oughton et al.* [2011] model assumes that $\mathbf{z}^{\pm}$ consists of two components, quasi-2D and wavelike (see Section 2.2 for more detail, and Subsection 2.3.1 for observational motivations for this approach), denoted by $\mathbf{q}^{\pm}$ and $\mathbf{w}^{\pm}$, respectively, such that

$$\mathbf{z}^{\pm} = \mathbf{q}^{\pm} + \mathbf{w}^{\pm}. \tag{3.3}$$

To further reduce the complexity of the above equations, *Oughton et al.* [2011] assume that the fluctuating components of the large scale fields (like the solar wind and Alfvén velocities) are

Z Quantity	Description	W Quantity
$Z_\pm^2 = \langle \mathbf{q}^\pm \cdot \mathbf{q}^\pm \rangle$	Elssässer energies	$W_\pm^2 = \langle \mathbf{w}^\pm \cdot \mathbf{w}^\pm \rangle$
$2Z^2 = Z_+^2 + Z_-^2$	$\propto$ total energy	$2W^2 = W_+^2 + W_-^2$
$\sigma_c = \dfrac{Z_+^2 - Z_-^2}{Z_+^2 + Z_-^2}$	normalised cross-helicity	$\tilde{\sigma}_c = \dfrac{W_+^2 - W_-^2}{W_+^2 + W_-^2}$
$\sigma_D = \dfrac{\langle \mathbf{q}^+ \cdot \mathbf{q}^- \rangle}{Z^2}$	normalised energy difference	$\tilde{\sigma}_D = \dfrac{\langle \mathbf{w}^+ \cdot \mathbf{w}^- \rangle}{W^2}$

Table 3.1: Relations of the quasi-2D and wavelike quantities, from *Oughton et al.* [2011].

incompressible. Large scale gradients are assumed to be directed solely in the radial direction, and the solar wind speed is assumed to be much greater than the Alfvén speed. This last assumption is fairly reasonable given heliospheric conditions, at least beyond 0.3 AU [*Kojima et al.*, 1991; *Gazis et al.*, 1994; *McComas et al.*, 2000] and within the termination shock. The assumption that a turbulent cascade can heat the solar wind is also made.

Further assuming three separate similarity scales (related to the correlation scales discussed in Section 2.2), as opposed to the single scale assumed by *Breech et al.* [2008], and making further assumptions as to the nature of the correlation functions and shear tensor (see *Breech et al.* [2008] for more detail as to these assumptions, as well as *Zank et al.* [2012]), *Oughton et al.* [2011] present a two-component turbulence transport model describing the radial evolution of several quantities pertaining to the energy range of the turbulence power spectrum, *viz.* the fluctuation energies, correlation scales, and normalised cross helicities associated with quasi-2D and wavelike fluctuations.

In this model half the total energy in the energy range associated with quasi-2D and wavelike fluctuations, henceforth respectively referred to as Z and W components, can be acquired by solving

$$\frac{dZ^2}{dr} = -\left[1 + M\sigma_D - C_{sh}^Z\right]\frac{Z^2}{r} - \frac{\alpha f}{V_{sw}}\frac{Z^3}{l} - \frac{2\alpha f_{ZW}^+}{V_{sw}}\frac{WZ^2}{l}\frac{1}{1+Z/W} + \frac{2\alpha X^+}{V_{sw}}, \tag{3.4}$$

where V_{sw} denotes the bulk solar wind velocity, and V_A the Alfvén speed calculated from the global HMF and density fields; and

$$\frac{dW^2}{dr} = -\left[1 + M\tilde{\sigma}_D - C_{sh}^W\right]\frac{W^2}{r} - \frac{\tilde{\alpha}\tilde{f}}{V_{sw}}\frac{ZW^2}{\lambda}\frac{2}{1+\lambda/l} - \frac{2\tilde{\alpha}(1-\tilde{\sigma}_c^2)}{V_{sw}}\frac{W^4\lambda_{c,s}}{\lambda^2 V_A} - \frac{2\alpha X^+}{V_{sw}} + \frac{\dot{E}_{PI}}{V_{sw}}, \tag{3.5}$$

with tildes denoting a quantity associated with the W component. The quantities Z and W can be related to the Elssässer energies $Z_\pm^2$ and $W_\pm^2$ corresponding to the velocities related by Equations 3.1 and 3.3, by

$$Z^2 = \frac{Z_+^2 + Z_-^2}{2} \text{ and } W^2 = \frac{W_+^2 + W_-^2}{2}, \tag{3.6}$$

which in turn relate to the various quantities pertinent to this model as indicated by Table 3.1. Note that the variances corresponding to each component can be rather simply acquired by solving, *e.g.*,

$$\delta B_{q2D}^2 = \frac{\mu_o \rho}{r_A + 1} Z^2 \tag{3.7}$$

with ρ the solar wind mass density, and μ_o the permeability constant [*Minnie*, 2006].

The quantities α and β in Equations 3.4 and 3.5 are de Kármán-Taylor constants [*de Kármán and Howarth*, 1938; *Taylor*, 1938] of order unity, where here it is assumed that $\alpha = 2\beta$, implying turbulent decay at constant Reynolds numbers [*Oughton et al.*, 2011]. The normalised energy difference, denoted by σ_D, is a measure of the balance between the magnetic and kinetic energies implicit to the fluctuations considered [*Perri and Balogh*, 2010], and can be related to the Alfvén ratio r_A (see Subsection 2.3.3) by

$$\sigma_D = \frac{r_A - 1}{r_A + 1}. \tag{3.8}$$

The term in square brackets on the right hand sides of both Equations 3.4 and 3.5 models various effects: firstly, Z^2/r and W^2/r model WKB-type effects (see *Oughton et al.* [2011]), while the mixing factor M describes the coupling of the small-scale fluctuations to gradients in large-scale fields like that of the heliospheric magnetic field [see, *e.g.*, *Oughton and Matthaeus*, 1995; *Breech et al.*, 2008]. The value of M depends on the assumed nature of the fluctuations, with $M = 1/3$ for isotropic fluctuations, and $M = \cos^2\psi$, where ψ denotes the winding angle of the heliospheric magnetic field, for transverse fluctuations [*Breech et al.*, 2008].

Lastly, the terms C_{sh}^Z and C_{sh}^W model driving due to large scale stream shear instabilities [*Breech et al.*, 2005; *Minnie*, 2006; *Breech et al.*, 2008; *Oughton et al.*, 2011]. In Eq. 3.4, the second term on the right hand side represents de Kármán and Howarth-Taylor decay of the Z fluctuations due to interactions with fluctuations of the same type, while the third term represents the decay of Z-type fluctuations due to interactions with W-type fluctuations. The second term in Eq. 3.5 describes the effects of weak turbulence, while the third-to-last term models an Iroshnikov-Kraichnan decay of W fluctuations (*Oughton et al.* [2011], and references therein). The term $\dot{E}_{PI}$ models the energy injected into the W fluctuations due to the formation of pickup ions, and will be discussed in more detail in a subsequent section. The terms in both equations involving the quantity X^+ (more on which below) describe the exchange of energy between the Z and W components. The various quantities denoted by f are attenuation factors, in that they model the weakening of nonlinear factors associated with larger values of the cross helicities associated with the Z and W components (here represented by σ_c and $\tilde{\sigma}_c$, respectively), and are related by

$$\begin{aligned} f &= f_{zz}^{+} \\ \tilde{f} &= f_{wz}^{+} \\ f' &= \sigma_c f_{zz}^{+} - f_{zz}^{-} \\ \tilde{f}' &= \tilde{\sigma}_c f_{wz}^{+} - f_{wz}^{-} \\ f_{zw}' &= \sigma_c f_{zw}^{+} - f_{zw}^{-}, \end{aligned} \tag{3.9}$$

where, denoting z and w with generic symbols a and b,

$$f_{ab}^{\pm} = \frac{1}{2}\left[(1+\sigma_c^a)\sqrt{1-\sigma_c^b} \pm (1-\sigma_c^a)\sqrt{1+\sigma_c^b}\right]. \tag{3.10}$$

Note that, for example, a superscript a on σ_c will represent $\tilde{\sigma}_c$ if $a = W$, and σ_c if $a = Z$, and similarly for b.

The correlation scale l perpendicular to the uniform component of the heliospheric magnetic field $\mathbf{B}_o$, and associated with the Z fluctuations, can be found by solving

$$\frac{dl}{dr} = -\hat{C}^Z_{sh}\frac{l}{r} + \frac{\beta}{V_{sw}}\left[fZ + f^+_{ZW}\frac{2W}{1+Z/W} - \frac{2lX^+}{Z^2}\right]. \tag{3.11}$$

The perpendicular correlation scale λ, associated with the W fluctuations, is given by

$$\frac{d\lambda}{dr} = -\hat{C}^W_{sh}\frac{\lambda}{r} + \frac{2\tilde{\beta}}{V_{sw}}\left[\frac{\tilde{f}Z}{1+\lambda/l} + (1-\tilde{\sigma}_c^2)\frac{W^2\lambda_{c,s}}{\lambda V_A} + \frac{\alpha\lambda X^+}{\tilde{\alpha}W^2}\right]. \tag{3.12}$$

Note that, as no observations currently exist to distinguish between the above quantities [*Oughton et al.*, 2011], the 2D correlation length is treated as a center-of-mass type average of l and λ, such that

$$\lambda_{c,2D} = \frac{Z^2 l + W^2\lambda}{Z^2 + W^2}. \tag{3.13}$$

The correlation scale $\lambda_{c,s}$ parallel to the background magnetic field, is yielded by

$$\frac{d\lambda_{c,s}}{dr} = -\hat{C}^W_{sh}\frac{\lambda_{c,s}}{r} + 2\tilde{\alpha}(1-\tilde{\sigma}_c^2)\frac{W^2\lambda_{c,s}^2}{V_{sw}V_A\lambda^2} - (\lambda_{c,s} - \lambda_{res})\frac{\dot{E}_{PI}}{V_{sw}W^2}, \tag{3.14}$$

where λ_{res} denotes a resonant parallel lengthscale. Energy that is generated in the formation of the pickup ions would appear in the wavelike component's spectrum at a lengthscale corresponding to λ_{res}, and is assumed to be inversely proportional to the proton gyrofrequency, such that

$$\lambda_{res} = \frac{2\pi V_{sw}}{\Omega_{ci}}, \tag{3.15}$$

following *Isenberg* [2005]. Here, as in *Oughton et al.* [2011], shear driving for each component is assumed to be approximately at the relevant correlation scale, implying that $\hat{C}^Z_{sh} = \hat{C}^W_{sh} = 0$.

The normalised cross-helicities σ_c and $\tilde{\sigma}_c$, associated with the quasi-2D and wavelike components respectively, are found by solving

$$\frac{d\sigma_c}{dr} = \frac{\alpha}{V_{sw}}\left[\frac{f'Z}{l} + \frac{f'_{ZW}W}{l}\frac{2}{1+Z/W} - \frac{2(\sigma_c X^+ - X^-)}{Z^2}\right] - \left[\frac{C^Z_{sh} - M\sigma_D}{r}\right]\sigma_c \tag{3.16}$$

and

$$\frac{d\tilde{\sigma}_c}{dr} = \frac{2\tilde{\alpha}}{V_{sw}}\left[\frac{\tilde{f}'}{1+\lambda/l}\frac{Z}{\lambda} + \tilde{\sigma}_c(1-\tilde{\sigma}_c^2)\frac{W^2\lambda_{c,s}}{\lambda^2 V_A}\right] + \frac{2\alpha(\tilde{\sigma}_c X^+ - X^-)}{V_{sw}W^2} - \left[\frac{C^W_{sh} - M\tilde{\sigma}_D}{r} + \frac{\dot{E}_{PI}}{V_{sw}W^2}\right]\tilde{\sigma}_c. \tag{3.17}$$

For the purposes of comparison to observations, a composite normalised cross helicity is defined as

$$\sigma_{c,comp} = \frac{Z^2\sigma_c + W^2\tilde{\sigma}_c}{Z^2 + W^2}. \tag{3.18}$$

The terms modelling the exchange of energy between the W and Z components are given by

$$X^{\pm} = \frac{1}{2}(Y^+ \pm Y^-), \tag{3.19}$$

where the quantities $Y^{\pm}$ are

$$Y^{\pm} = W_{\pm} Z_{\pm} \left[\frac{Z_{\mp}}{\lambda} \Gamma_{w}^{z_{\mp} w_{\pm}} + \frac{W_{\mp}}{\lambda} \Gamma_{w}^{w_{\mp} w_{\pm}} - \frac{Z_{\mp}}{l} \Gamma_{w}^{z_{\mp} z_{\pm}} - \frac{W_{\mp}}{l} \Gamma_{w}^{w_{\mp} z_{\pm}} \right]. \tag{3.20}$$

Furthermore,

$$\Gamma_{c}^{ab} = \frac{1}{1 + \tau_{nl}^{ab} / \tau_{A}^{c}}, \tag{3.21}$$

where τ_{nl}^{ab} and τ_{A}^{c} are, respectively, the nonlinear and Alfvén times discussed in Subsection 2.2.4, following the same notation as that employed for Equation 3.10. These quantities, then, are expressed by [*Oughton et al.*, 2006; *Oughton et al.*, 2011]

$$\begin{aligned} \tau_{A}^{w} &= \frac{\lambda_{c,s}}{V_A}, \\ \tau_{nl}^{ww} &= \frac{\lambda}{W}, \\ \tau_{nl}^{zz} &= \frac{l}{Z}, \\ \tau_{nl}^{zw} &= \frac{\lambda}{Z}, \\ \tau_{nl}^{wz} &= \frac{l}{W}. \end{aligned} \tag{3.22}$$

Note that the above renditions of $X^{\pm}$ denote the full expression as given in Appendix A of *Oughton et al.* [2011].

Lastly, the solar wind (proton) temperature can be solved for by utilizing

$$\frac{dT}{dr} = -\frac{4}{3}\frac{T}{r} + \frac{m_p}{3 V_{sw} k_B} \left[\alpha \left(\frac{f Z^3}{l} + \frac{2 f_{ZW}^{+}}{1 + Z/W} \frac{W Z^2}{l} \right) + 2\tilde{\alpha} \left(\frac{\tilde{f}}{1 + \lambda/l} \frac{Z W^2}{\lambda} + (1 - \tilde{\sigma}_c^2) \frac{W^4 \lambda_{c,s}}{\lambda^2 V_A} \right) \right], \tag{3.23}$$

where the first term denotes adiabatic heat losses, and the last two heat gains due to the dissipation of energy in both the quasi-2D and wavelike components here considered. Note that the effects of heat conduction are not included in Eq. 3.23.

The model described above is solved numerically in this study, by utilizing a 4th-order Runge-Kutta method [see, *e.g.*, *Cheney and Kinkaid*, 1999]. The particulars of such a solution depend on the boundary conditions assumed, the modelling of the various terms in the above equations, such as the shear term C_{sh}, and the choices made as to the behaviour of large-scale quantities in the heliosphere. These will be the topic of the next section.

3.3 Inputs to the *Oughton et al.* [2011] model

This section begins with brief discussions, and motivations, of how the various inputs to the *Oughton et al.* [2011] model are treated in the present study. A set of boundary conditions will then be proposed which include fits to turbulence quantities along the actual *Ulysses* trajectory, in contrast to the usual ecliptic/high latitude approach. In terms of the large scale fields, these quantities will be modelled so as to mimic observed solar minimum conditions as closely as possible.

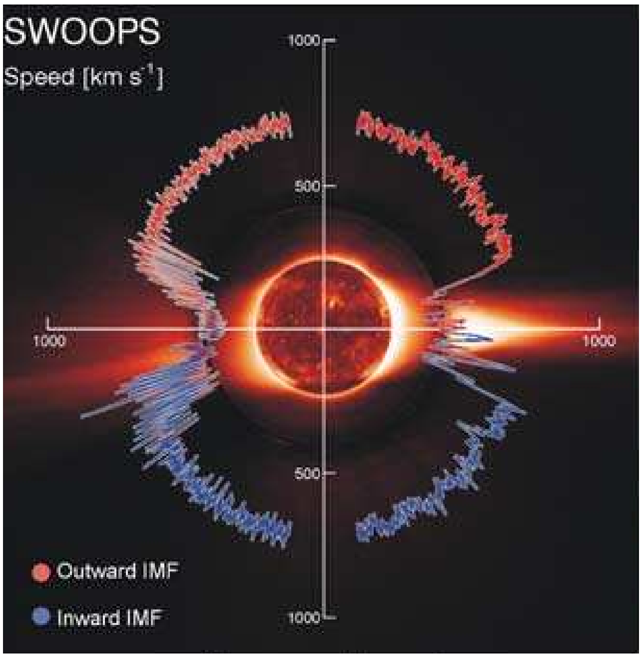

Figure 3.1: Solar wind structure as observed by *Ulysses* during solar minimum conditions [*McComas et al.*, 2003].

3.3.1 Large-scale fields

In this study, large-scale heliospheric quantities are set so as to represent generic solar minimum conditions observed for the last few solar cycles. The solar wind speed, beyond approximately 0.3 AU, is observed to be almost constant as a function of radial distance [*Kojima et al.*, 1991; *Gazis et al.*, 1994]. At the heliospheric termination shock, however, a sharp decrease in the solar wind speed is observed at heliocentric radial distances of ~ 94 and ~ 84 AU respectively by the *Voyager 1* and 2 spacecraft [see, *e.g.*, *Stone et al.*, 2005; *Stone*, 2007; *Jokipii*, 2008]. For the purposes of the present study, an inner boundary of 0.3 AU and an outer boundary of 100 AU are assumed for a spherical heliosphere with no termination shock, as in, *e.g.*, *Breech et al.* [2008] and *Oughton et al.* [2011]. The solar wind speed, during solar minimum, also displays a marked latitudinal dependence, with a speed of $\sim$ 800 km/s over the solar poles and $\sim$ 400 km/s in the ecliptic, with the transition occurring at intermediate latitudes [see, *e.g.*, *Phillips et al.*, 1995; *McComas et al.*, 2000; *McComas et al.*, 2003], illustrated in Figure 3.1.

This latitudinal dependence will be modelled using a hyperbolic tangent function,

$$V_{sw}(\theta) \quad = \quad 400\,\mathrm{km/s}\begin{cases} 1.5 - 0.5\tanh\left[8\left(\theta - \pi/2 + \alpha + \delta_t\right)\right] & \text{if } \theta \leq \pi/2; \\ 1.5 + 0.5\tanh\left[8\left(\theta - \pi/2 - \alpha - \delta_t\right)\right] & \text{if } \theta > \pi/2 \end{cases} \tag{3.24}$$

with α the tilt angle of the heliospheric current sheet, θ colatitude and $\delta_t = 20\pi/180$ radians. The factor of 8 governs the steepness of the transition of the function. The above latitudinal profile is illustrated later in Figure 3.6.

The solar wind proton density ρ is assumed to scale as r^{-2}. At Earth, the solar wind density ranges in value from $\sim 5 - 10$ /cc [see, e.g., *Smith et al.*, 2001; *Wang et al.*, 2007], and is chosen to

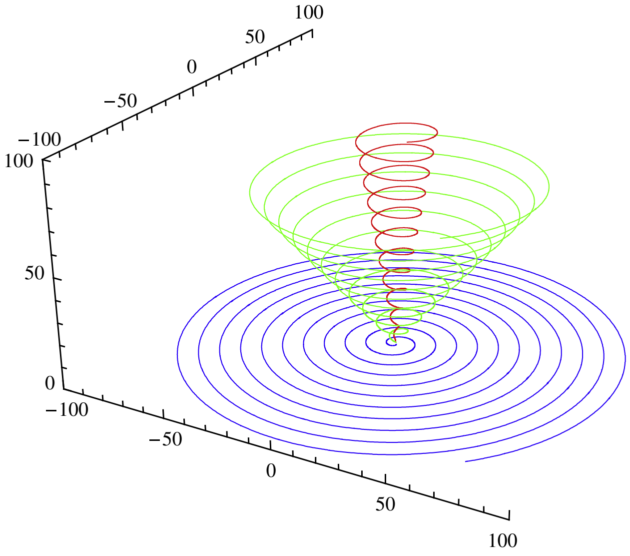

Figure 3.2: Some Parker heliospheric magnetic field lines, originating at $10°$, $40°$, and $90°$ colatitude [*Engelbrecht and Burger*, 2010].

be 7 /cc. Furthermore, the density at Earth is assumed to decrease with increasing solar wind speed, so as to assume a value of 2.7 /cc over the poles [see, e.g., *McComas et al.*, 2000].

Two models for the heliospheric magnetic field are here considered: that of *Parker* [1958], and the Schwadron-Parker hybrid field proposed by *Hitge and Burger* [2010]. The Parker model, albeit the simplest of several proposed HMF models, is in fair agreement with magnetic observations in the ecliptic plane [see, *e.g.*, *Klein et al.*, 1987]. In the derivation of this model the solar wind outflow is assumed to be spherically symmetric, with a perfect alignment of the solar magnetic and rotational axes. The solar plasma is assumed to rotate rigidly, from the inner corona to the Alfvén radius at $\sim 10r_\odot$, at a constant rate Ω. Assuming a source surface at a distance $r_{ss} = 10r_\odot$ beyond which the heliospheric magnetic field is 'frozen' into the solar wind flow, and where the solar wind flow is directed radially outward, the various components of the Parker HMF in heliocentric coordinates are given by

$$\begin{aligned} B_r &= A\left(\frac{r_e}{r}\right)^2 \\ B_\theta &= 0 \\ B_\phi &= -B_r\frac{\Omega(r-r_{ss})}{V_{SW}}\sin\theta. \end{aligned} \tag{3.25}$$

Here A is a constant denoting the magnitude of the radial component of the field at Earth. The sign of A indicates the polarity of the field, in that a positive sign implies that the field in the northern hemisphere points away from the sun, while pointing inward in the southern hemisphere. Quantities of order r_{ss}/r will be neglected in what follows in order to facilitate direct comparison with the Schwadron-Parker field. In the present study, a value of 5 nT is assumed for the magnetic field magnitude at Earth, as is commonly used in modulation studies pertaining to solar minimum conditions [see, *e.g.*, *Jokipii*, 2001; *Ferreira et al.*, 2003; *Caballero-*

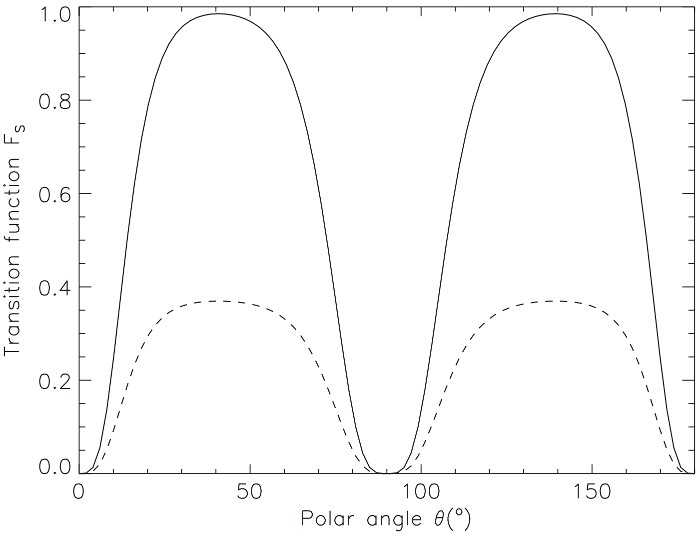

Figure 3.3: Transition functions for the Schwadron-Parker hybrid field used by *Sternal et al.* [2011]. Solid line denotes the full transition function of Eq. 3.28, dashed the reduced transition functions. These transition functions are equal to the square root of the transition function given by Eq. 3.28.

Lopez et al., 2004; *Caballero-Lopez et al.*, 2004a]. The Parker spiral, or winding, angle is defined as the angle between the radial and azimuthal components of the HMF,

$$\tan\psi \equiv -\frac{B_\phi}{B_r} = \frac{\Omega r}{V_{sw}} \sin\theta. \tag{3.26}$$

Due to the lack of a meridional component, Parker field lines spiral along cones of constant colatitude, as shown in Figure 3.2. Various observationally motivated modifications exist for the standard Parker model at higher heliolatitudes [see, *e.g.*, *Jokipii and Kóta*, 1989; *Smith and Bieber*, 1991], but are not considered in the present study.

Unexpectedly low cosmic-ray intensities [see, *e.g.*, *Simpson et al.*, 1996; *Heber et al.*, 1996; *Heber et al.*, 2008] and recurrent variations [see, *e.g.*, *Kunow et al.*, 1995; *Simpson et al.*, 1995; *Zhang*, 1997; *Paizis et al.*, 1999; *Dunzlaff et al.*, 2008] observed by the *Ulysses* spacecraft in the polar regions of the heliosphere implied a possibly more complex structure for the heliospheric magnetic field. *Fisk* [1996], assuming superradial expansion of field lines beyond the source surface and incorporating the observed [see, *e.g.*, *Snodgrass*, 1983] differential rotation of the photosphere, proposed a model for the HMF with a strong meridional component [see also *Zurbuchen et al.*, 1997]. Furthermore, *Burger and Hitge* [2004] and *Burger et al.* [2008] proposed Fisk-Parker hybrid models, equivalent to the Parker field in the ecliptic region and directly over the solar poles (based on the assumption of no differential rotation at the highest solar latitudes [*Schou et al.*, 1998]), but equal to the Fisk field derived by *Zurbuchen et al.* [1997] in regions of intermediate latitude, that could in principle explain the cosmic ray observations of *Zhang* [1997] [see, *e.g.*, *Burger et al.*, 2008; *Engelbrecht and Burger*, 2010].

Three-dimensional, time-dependent MHD simulations performed by *Lionello et al.* [2006] do indeed confirm the basic ideas behind Fisk-type fields, but direct evidence for the existence

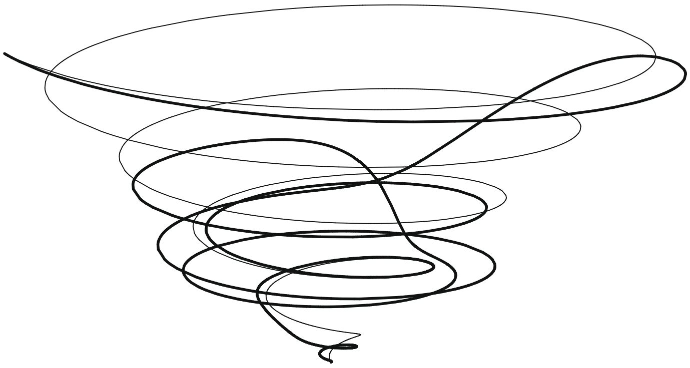

Figure 3.4: Field lines originating at the same heliolatitude and longitude for the Parker (thin line) and Schwadron-Parker (thick line) heliospheric magnetic field models, from *Hitge and Burger* [2010]. Note that the field lines shown originate at a heliolatitude corresponding to a region where the solar wind speed exhibits a large latitude gradient.

of such fields appears to be ambiguous. *Zurbuchen et al.* [1997]'s analysis of *Ulysses* magnetic field data strongly suggested to those authors the existence of a Fisk-type field, but *Forsyth et al.* [2002] concluded that a reliable detection of such a field would be rendered difficult by the low amplitude of the systemic deviations characteristic of a Fisk-type field, and *Burger et al.* [2008] argue that even periodicities expected of the azimuthal component of the Parker field are not to be seen in the Ulysses data, possibly being masked by the very action of the motion of the HMF footpoints. Furthermore, *Roberts et al.* [2007] find no evidence for a Fisk-type field, but concede that their conclusions are based on the possibly overestimated Fisk field parameters of *Zurbuchen et al.* [1997]. *Sternal et al.* [2011], however, model the transport of low-energy electrons, and find that the use of a Schwadron-Parker hybrid field (discussed below) can yield periodicities observed for such electrons by Ulysses, albeit with a moderate 'Fisk-effect'.

A limitation of the Fisk-type fields described above, is that they are divergence-free only if a constant solar wind speed is assumed, a problem addressed by *Schwadron* [2002] and *Schwadron and McComas* [2003]. *Hitge and Burger* [2010] propose a Schwadron-Parker hybrid model, such that

$$\begin{aligned} B_r &= \frac{A}{r^2}\left(1+\frac{r}{V_{sw}^2}\omega^*\sin\beta^*\sin\phi^*\frac{dV_{sw}}{d\theta}\right) \\ B_\theta &= \frac{A}{rV_{sw}}\omega^*\sin\beta^*\sin\phi^* \\ B_\phi &= \frac{A}{rV_{sw}}\left[\omega^*\cos\beta^*\sin\theta+\frac{d}{d\theta}\left(\omega^*\sin\beta^*\sin\theta\right)\cos\phi^*-\Omega\sin\theta\right] \end{aligned} \tag{3.27}$$

where $\phi^* = \phi + \Omega r/V_{sw} - \phi_0$ and ϕ_0 a constant. Furthermore, $\omega^* = \omega/4F_s$ with ω the differential rotation rate of the HMF footpoints, here assumed to be constant and equal to $\Omega/4$, $\beta^* = \beta F_s$ a parameter that governs the non-radial expansion of magnetic field lines in the region between the photosphere and source surface [see *Burger et al.*, 2008, for more detail], and F_s a latitude-dependent transition function defined so that the above field is a pure Schwadron field should

$F_s = 1$, and a pure Parker field should $F_s = 0$, and is given by

$$F_S = \begin{cases} \{\tanh[\delta_p \theta] + \tanh[\delta_p(\theta - \pi)] - \tanh[\delta_e(\theta - \theta'_b)]\}^4 & \text{if } \theta \in [0, \theta'_b); \\ 0 & \text{if } \theta \in [\theta'_b, \pi - \theta'_b]; \\ \{\tanh[\delta_p \theta] + \tanh[\delta_p(\theta - \pi)] - \tanh[\delta_e(\theta - \pi - \theta'_b)]\}^4 & \text{if } \theta \in (\pi - \theta'_b, \pi]. \end{cases} \tag{3.28}$$

Here $\delta_p = 5.0 = \delta_e$ are constants affecting the gradients of F_S, their values being chosen so as to coincide with those of *Burger et al.* [2008] and *Sternal et al.* [2011], and $\theta'_b = 80/180\pi$. The reduced transition function proposed by *Sternal et al.* [2011], where $F'_S = 3/8F_S$, is used in the present study. Both transition functions, reduced and that of Eq. 3.28, are illustrated as functions of latitude in Fig. 3.3. A representation of a Schwadron-Parker field line (using the full transition function of Eq. 3.28), along with a Parker field line originating at the same heliolatitude, is shown in Fig. 3.4. The winding angle for such Fisk-type fields is given by [*Burger et al.*, 2008]

$$\tan\psi \equiv -\frac{B_\phi}{\sqrt{B_r^2 + B_\theta^2}}, \tag{3.29}$$

which reduces to the standard expression of Eq. 3.26 should a Parker-type field be used.

Lastly, the Alfvén speed is calculated using the assumed model for the heliospheric magnetic field, and the solar wind proton density discussed earlier.

3.3.2 Turbulence related model inputs

This subsection aims to describe and motivate how the various terms affecting the evolution of the small-scale turbulence quantities described by the *Oughton et al.* [2011] model are treated in the present as well as in some previous studies.

The de Kármán-Taylor constants

The de Kármán-Taylor constants assumed in the present study follow one of the choices of *Pei et al.* [2010a], where $\alpha = 0.125$, with the assumption of turbulent decay at constant Reynolds numbers, such that $\alpha = 2\beta$ [*Oughton et al.*, 2011], as opposed to the choice of $\alpha = 0.25$ made by *Oughton et al.* [2011], who follow that made by *Breech et al.* [2009]. This approach is motivated by the need to find model agreement with newer turbulence observations than those considered by *Oughton et al.* [2011] (see Subsection 3.3.3 for more detail). Furthermore, the analogues to these constants, $\tilde{\alpha}$ and $\tilde{\beta}$, found in the equations governing wavelike quantities, are here assumed to be equal to the de Kármán-Taylor constants in the equations governing the quasi-2D quantities [*Oughton et al.*, 2011]. In previous studies using related models, the assumption that $\alpha = 0.8$ was made [see, *e.g.*, *Breech et al.*, 2005, 2008], while *Pei et al.* [2010a], employing the *Breech et al.* [2008] model, consider two options, $\alpha = 0.25$, and $\alpha = 0.125$.

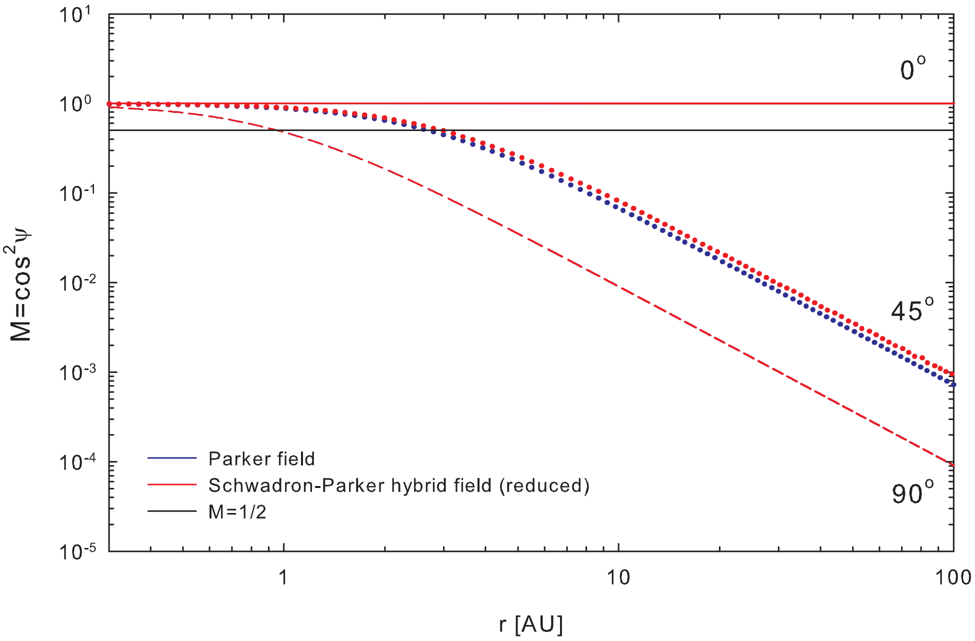

Figure 3.5: The geometric mixing factor M as a function of heliocentric radial distance at various colatitude, for both a Parker field and a reduced Schwadron-Parker hybrid field. Line types for the two HMF models denote colatitude: solid lines $0°$, dotted lines $45°$ and dashed lines $90°$.

The geometric mixing factor

The geometrical mixing term is in this study taken to be $M = \cos^2\psi$, and is in this study allowed to vary throughout the heliosphere, with the HMF winding angle being calculated from Eq. 3.29. This is different from the approach taken in previous studies where M was assumed to be equal to $1/2$ throughout the heliosphere, a value corresponding to the magnitude of the winding angle at Earth. This quantity is illustrated at various colatitudes and as a function of radial distance for both HMF models here considered, in Fig. 3.5. Over the poles (solid lines), and in the ecliptic plane (dashed lines), both magnetic field models yield the same result, as expected from the action of the transition function discussed in the above subsection. At a colatitude of $45°$ (dotted lines), however, some slight difference in the geometric mixing terms yielded can be seen, due to the transition function being quite close to its maximum value at this colatitude, and hence the hybrid field being at its most Fisk-like. Note that the factor M reaches its maximum value at the poles. The uniform value of $1/2$ assumed in previous studies is also shown in Fig. 3.5 to illustrate the significant differences between it and the calculated values for this quantity, especially beyond a few AU.

The Alfvén ratio and normalised energy difference

The Alfvén ratio r_A is in the present study assumed to remain constant at a value of 0.5, an assumption motivated by the observations of, amongst others, *Roberts et al.* [1987a, b] (see

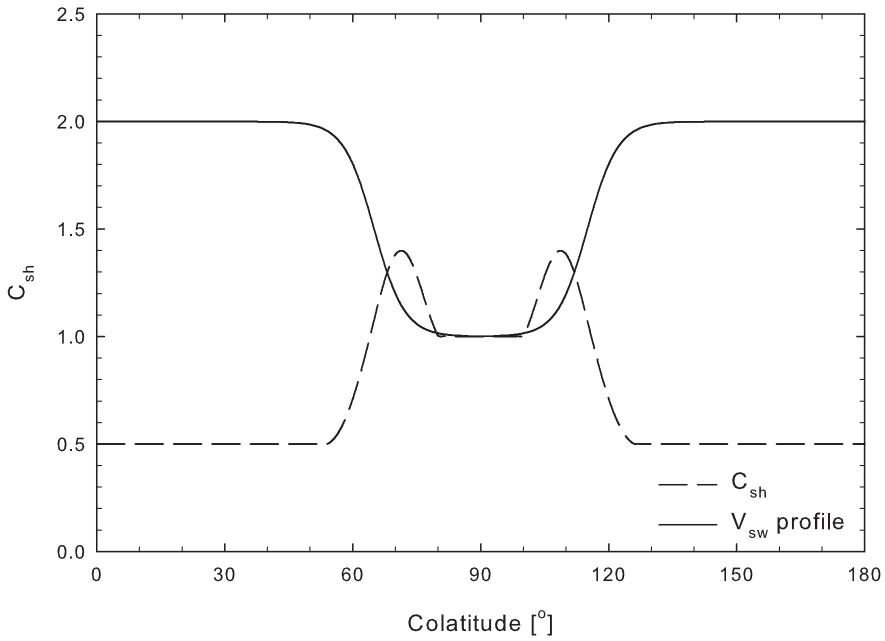

Figure 3.6: Solar wind and C_{sh} profiles used in the present study, as functions of colatitude.

Subsection 2.3.3 for more detail), and made following, *e.g.*, *Breech et al.* [2008]; *Pei et al.* [2010a]; *Oughton et al.* [2011]. By Eq. 3.8, the choice of Alfvén ratio has implications for the value of the normalised energy difference σ_D, which here then assumes a value of $-1/3$. Note that the wavelike analogue to the normalised energy difference, denoted by $\tilde{\sigma}_D$, is assumed to be equal to σ_D.

The stream-shear term

In the present study, it is assumed that $C_{sh}^Z = C_{sh}^W = C_{sh}$, again following the approach of *Oughton et al.* [2011]. In turn, C_{sh} is modelled using a latitudinal dependence very similar the profile used by *Breech et al.* [2008], who provide an estimation for this constant,

$$C_{sh} = \frac{\Delta V_{sw}}{V_{sw}} \frac{r}{\Delta r}, \tag{3.30}$$

where ΔV_{sw} denotes the latitudinal change in the solar wind speed, and Δr the scale across which neighbouring streams interact [see also *Zhou and Matthaeus*, 1990; *Zank et al.*, 1996].

The profile used in this study is essentially equal to that used by *Breech et al.* [2008] and is illustrated in Fig. 3.6. Below a colatitude of $\sim 55°$ and above $\sim 125°$, the shear constant is assumed to have a value of 0.5 [*Breech et al.*, 2005], while in the ecliptic plane it is assumed to be equal to one [*Matthaeus et al.*, 2004]. Technically, according to Eq. 3.30, a solar wind profile such as that used in this study (see Eq. 3.24) should yield negligibly small shear constants over the poles and in the ecliptic plane. The shear profiles used were artificially set to the values used for these regions by *Breech et al.* [2008] to model the shear constant in such a way as to allow for comparisons to previous work, while at the same time retaining a solar wind profile commonly used in cosmic-ray modulation studies for exactly the same reason. At intermediate colatitudes, however, the shear profile used in this study is calculated using the change in latitude of the solar wind speed given by Eq. 3.24, and increases to a value of ~ 1.4, due to the increased shear in this region. Note that in this region the profile used here departs slightly in magnitude from that used by *Breech et al.* [2008] due to the different solar wind profile used in its calculation. No radial dependence is assumed for the stream-shear constant in this study, as in *Breech et al.* [2008]. This omission is probably unrealistic, as the scale Δr might vary with increasing heliocentric radial distance, but no observations currently exist to constrain any such radial dependence.

The pickup ion energy injection term

The last turbulence-related input to consider is the energy injected by the formation of pickup ions (see Subsection 2.3.7 for more detail). *Breech et al.* [2005, 2008] follow the approach employed by, *e.g.*, *Smith et al.* [2001] and *Smith et al.* [2006b], based on the results of *Williams and Zank* [1994], and use

$$\dot{E}_{PI} = f_D \frac{V_{sw} V_A n_H}{\tau_{ion} n_{sw}} \exp\left[-(L_{cav}/r)(\theta_n/\sin\theta_n)\right], \tag{3.31}$$

where n_{sw} and τ_{ion} denote respectively the solar wind proton density, and the neutral ionization time at Earth; n_H the neutral hydrogen density at the termination shock; L_{cav} the radial heliocentric extent of the ionization cavity; and f_D a scaling factor. The angle θ_n is measured between an observation point and the neutral hydrogen upstream direction. Equation 3.31 assumes a cold neutral hydrogen density [*Vasyliunas and Siscoe*, 1976], which may not be the best choice of model [see, *e.g.*, *Zank*, 1999], and is not the most realistic of scenarios given recent *IBEX* results [see, *e.g.*, *Fuselier et al.*, 2009]. This model, however, has the benefit of being relatively tractable and has yielded good agreement with solar wind proton temperature observations when used in conjunction with turbulence transport models [see, *e.g.*, *Smith et al.*, 2001; *Isenberg*, 2005; *Smith et al.*, 2006b; *Isenberg et al.*, 2010].

The pickup energy source term employed here is that used by *Oughton et al.* [2011], who, following *Isenberg* [2005], apply a slightly different but nevertheless equivalent form of Eq. 3.31,

$$\dot{E}_{PI} = \zeta \frac{V_{sw}^2 n_H}{\tau_{ion} n_{sw}} \exp\left[-(L_{cav}/r)(\theta_n/\sin\theta_n)\right]. \tag{3.32}$$

Here ζ is also a scaling factor, denoting the fraction of the pickup ion energy that goes to the fluctuations generated. The scaling factors in the two above equations are related by

$$f_D = \frac{V_{sw}}{V_A}\zeta, \tag{3.33}$$

where ζ is found from first principles by *Isenberg et al.* [2003] and *Isenberg* [2005] to be of the order of a few percent. In the present study, ζ is assumed to be constant and equal to 0.04,

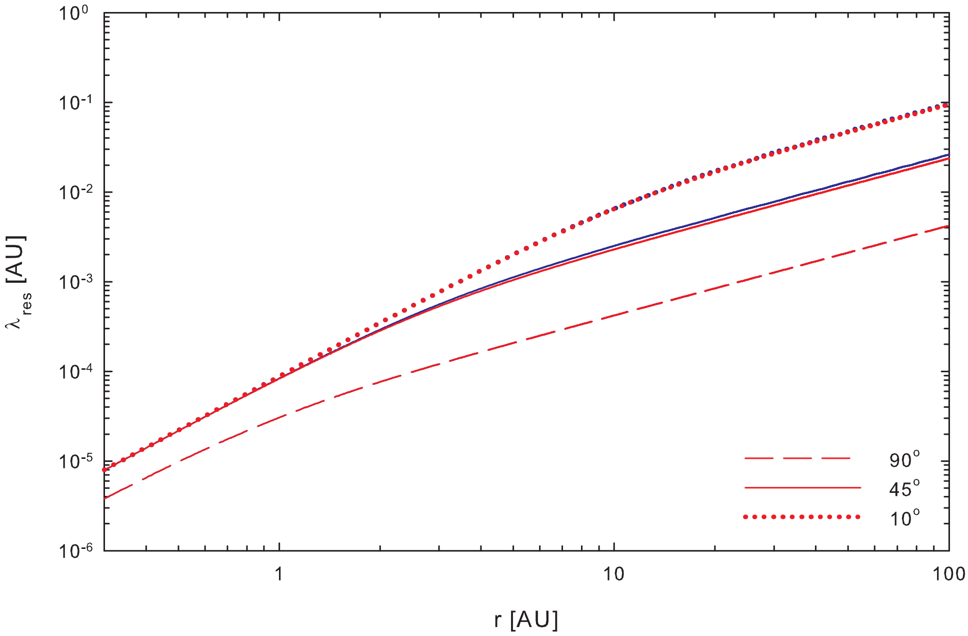

Figure 3.7: The resonant lengthscale λ_{res}, as function of radial distance, at various colatitudes for both a Parker (red line types) and a reduced Schwadron-Parker hybrid field (blue line types).

following the choice of *Oughton et al.* [2011]. Furthermore, a value of $0°$ is here assumed for θ_n, thereby implying a spatially uniform influx of neutral hydrogen, a standard approach followed by many authors using this type of model [see, *e.g.*, *Smith et al.*, 2001; *Breech et al.*, 2008; *Pei et al.*, 2010a; *Oughton et al.*, 2011].

A value of 0.1 /cc is chosen for n_H, as in *Breech et al.* [2008]; *Oughton et al.* [2011], following the results of line-of-sight observations of nearby stellar Lyman-α emission lines [see, *e.g.*, *Anderson et al.*, 1978; *Gry and Jenkins*, 2001]. However, various Lyman-α observations by other studies indicate that this parameter varies within a range of about $0.05 - 0.3$ /cc [*Scherer et al.*, 1999]. The ionization cavity size L_{cav} appears dependent upon the solar cycle [*Smith et al.*, 2001], and two values are commonly used as inputs for turbulence transport models: $L_{cav} = 5.6$ AU [see, *e.g.*, *Isenberg et al.*, 2003; *Isenberg*, 2005; *Isenberg et al.*, 2010], and $L_{cav} = 8$ AU [see, *e.g.*, *Smith et al.*, 2001; *Breech et al.*, 2008; *Usmanov et al.*, 2009]. *Schwadron and McComas* [2010], however, state that most incoming neutral hydrogen atoms would be ionized within ~ 4 AU. The present study assumes a value of 5.6 AU, following *Oughton et al.* [2011]. As to the neutral ionization time τ_{ion}, a constant value of 1.33×10^6 s is chosen [see, *e.g.*, *Smith et al.*, 2006b], although this parameter, too, varies with the solar cycle [*Smith et al.*, 2001].

The resonant lengthscale λ_{res} at which some of the energy due to the formation of pickup-ions is injected into the wavelike fluctuation spectrum is in this study modelled according to Eq. 3.15, so that it is proportional to the solar wind speed, and inversely proportional to the proton gyrofrequency. This quantity is illustrated at various colatitudes for both a Parker and a reduced Schwadron-Parker HMF as a function of radial distance, in Fig. 3.7. Clearly, λ_{res} increases from the ecliptic to the poles for both HMF models. Due to the action of the transition function, the results for the Parker and reduced Schwadron-Parker fields close to the poles (dotted lines) and in the ecliptic plane (dashed lines) are identical, and even at 45° colatitude (where the reduced Schwadron-Parker field, by the action of the transition function, should yield a result that deviates most from that of the Parker model) the differences between these models is very small, a result echoing those for the geometric mixing factor shown in Fig. 3.5.

3.3.3 Boundary values assumed

A proper choice of boundary values is crucial to any attempt at finding agreement between model outputs and spacecraft data. Due to the relatively recent publication of the *Oughton et al.* [2011] transport model, there aren't many sets of boundary conditions currently published, as is the case, for example, with the *Breech et al.* [2008] model. The boundary values assumed at 0.3 AU in the ecliptic plane, for both the present study and those used by *Oughton et al.* [2011], are listed in Table 3.2. The values chosen in this study are somewhat different to those used by *Oughton et al.* [2011], the main reason for this being that the boundary values for the various lengthscales were here set so as to agree with the newest observational values at Earth for these quantities reported by *Weygand et al.* [2011], whereas the boundary values used by *Oughton et al.* [2011] were set so as to agree to the 1 AU observations reported by *Weygand et al.* [2009]. These changes, due to the nature of the equations to be solved, necessitated further changes in the boundary values chosen for other quantities, such as the fluctuation energies. Furthermore, boundary values for the respective fluctuation energies were chosen so that (half) the total variance at Earth would agree with the solar minimum 6 nT^2 value from *Smith et al.* [2006b]. The boundary values for the quasi-2D fluctuation energy at 1 AU were chosen so that Z^2 accounts for approximately 80% of the total energy, as observed by *Bieber et al.* [1994]. This latter requirement was made following the approach outlined by *Oughton et al.* [2011]. The boundary values chosen for the respective normalised cross-helicities are the same as those chosen by *Breech et al.* [2008]. The enhanced values of the fluctuation energies, however, motivated a lower choice for the initial value of the solar wind proton temperature than that used by *Oughton et al.* [2011], as well as requiring a different choice of de Kármán-Taylor constants. Due to the observed solar cycle variability of observed turbulence quantities [see, *e.g.*, *Wicks et al.*, 2010; *Coburn et al.*, 2012], it must be emphasized that these boundary conditions were set so as to agree with solar minimum turbulence data wherever possible.

The purposes of the present study require a set of boundary values leading to a set of solutions throughout the heliosphere, which in turn requires a study similar to that of *Breech et al.* [2008]. However, *Oughton et al.* [2011] only provide a set of boundary conditions applicable to solar ecliptic conditions, therefore the boundary conditions here presented for high latitudes in a sense represent a first look at how successful the two-component turbulence transport model

Quantity	Unit	*Oughton et al.* [2011]	This study
Z^2	km^2/s^2	1500	1250
W^2	km^2/s^2	150	350
λ	AU	0.008	0.004
l	AU	0.008	0.004
$\lambda_{c,s}$	AU	0.036	0.011
σ_c	none	0.6	0.6
$\tilde{\sigma}_c$	none	0.6	0.6
T	K	1.6×10^6	2×10^5

Table 3.2: Boundary values assumed at 0.3 AU for the two-component turbulence transport model, in the slow solar wind.

Quantity	Unit	This study
Z^2	km^2/s^2	1600
W^2	km^2/s^2	3000
λ	AU	0.015
l	AU	0.015
$\lambda_{c,s}$	AU	0.011
σ_c	none	0.8
$\tilde{\sigma}_c$	none	0.8
T	K	1.6×10^6

Table 3.3: Boundary values assumed at 0.3 AU for the two-component turbulence transport model, in the fast solar wind.

is in reproducing high-latitude turbulence observations. The boundary values here used at the highest latitudes are listed in Table 3.3, with the latitudinal transition from the values assumed at low latitudes effected by means of the latitudinal solar wind profile assumed in this study, following the approach employed by *Breech et al.* [2008]. The various latitudinal profiles for the boundary values here used are illustrated as functions of colatitude in Fig. 3.8.

There are considerably less observational data available at high latitudes than in the ecliptic, and this study relies rather heavily on the observations of the fluctuation energies, correlation scales, normalised cross-helicities and solar wind proton temperatures taken by the *Ulysses* spacecraft, reported by *Bavassano et al.* [2000a, b], and discussed in Section 2.3. The primary motivation behind the choices of inner boundary values here made has been to find agreement with these *in situ* datasets *along the trajectory* of the *Ulysses* spacecraft. This approach to finding boundary values at high latitudes for turbulence transport models has not been taken before. *Bavassano et al.* [2000b] note that the turbulence in the high-latitude fast solar wind does not behave too differently to that present in low-latitude fast solar wind streams, and some of the choices made here take into account observations at Earth for such solar wind conditions. Inner boundary values for the wavelike and quasi-2D fluctuation energies were taken to assure a wavelike dominated anisotropy, motivated by the findings of *Dasso et al.* [2005] and *Weygand et al.* [2011], although it is unclear as to what the exact proportions of the anisotropy are (see Subsection 2.3.1 for a more detailed account). Likewise, boundary values for the correlation scales were so chosen so that model outputs would agree with correlation scales observed *along* the *Ulysses* trajectory. The boundary values for the correlation scales were also chosen so that the ratio of the wavelike correlation scale to the composite transverse scale (in the notation

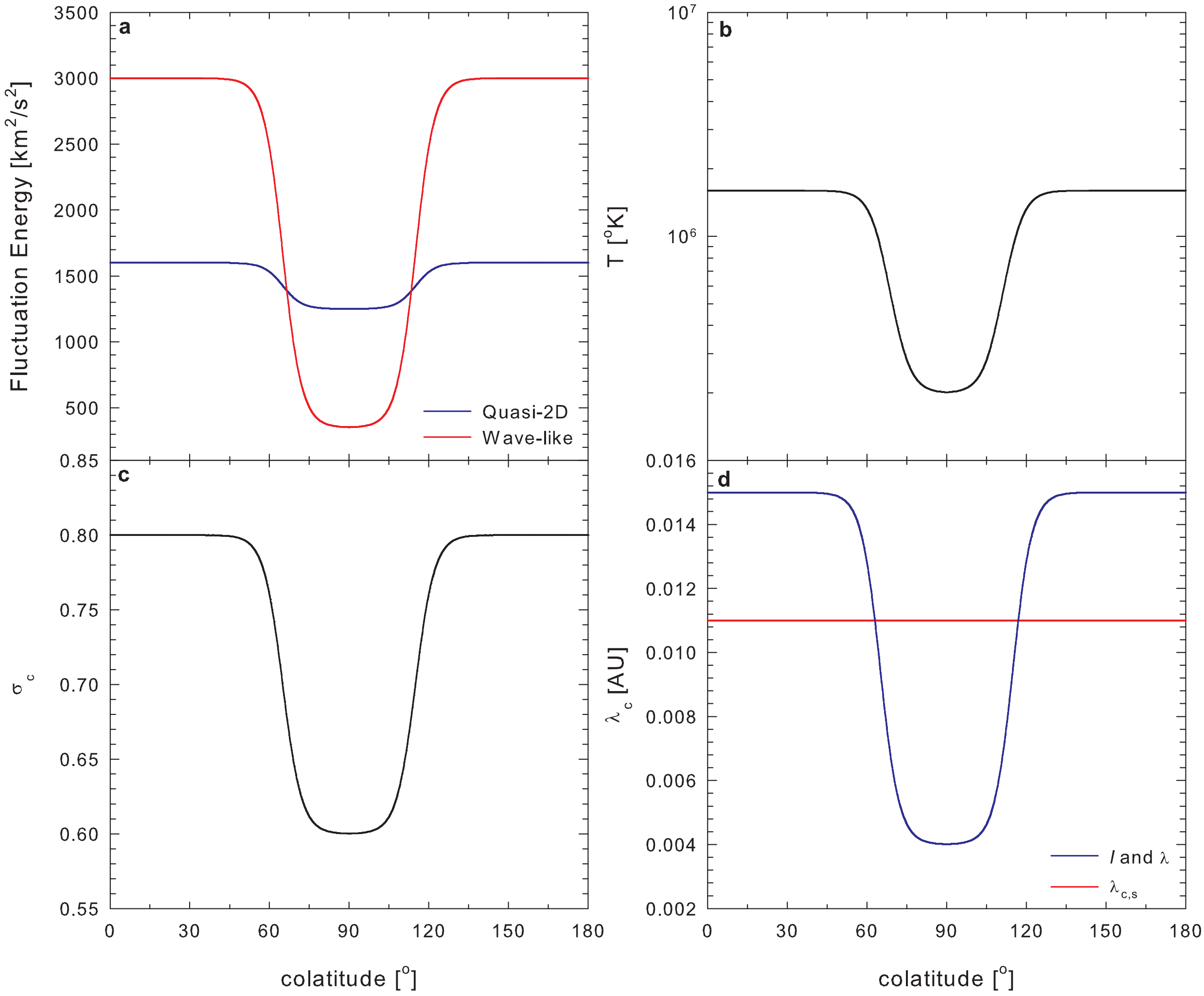

Figure 3.8: Boundary values for the *Oughton et al.* [2011] model assumed in the present study at 0.3 AU, as functions of colatitude. Note that the same boundary values are assumed for both σ_c, and $\tilde{\sigma}_c$.

here used, $\lambda_{c,s}/\lambda_{c,2D}$) yielded by the transport model would agree with the findings of *Dasso et al.* [2005] and *Weygand et al.* [2011]. The values found by *Weygand et al.* [2011] for fast solar wind conditions at Earth are, however, considerably lower than the observations of *Bavassano et al.* [2000a, b]. These latter observations were *in situ*, however, and so emphasis was placed on finding broad agreement with them, and not with the *Weygand et al.* [2011] findings.

3.4 Solutions to the two-component turbulence transport model

The equations that constitute the two-component turbulence transport model are solved using a standard 4th-order Runge-Kutta scheme, assuming 570 radial, 301 meridional, and 67 azimuthal gridpoints. Except where otherwise noted, a Parker field and a spherically symmetric pickup-ion source term is employed. This approach implies axially symmetric solutions, and the solutions presented below are taken arbitrarily at 0° azimuth.

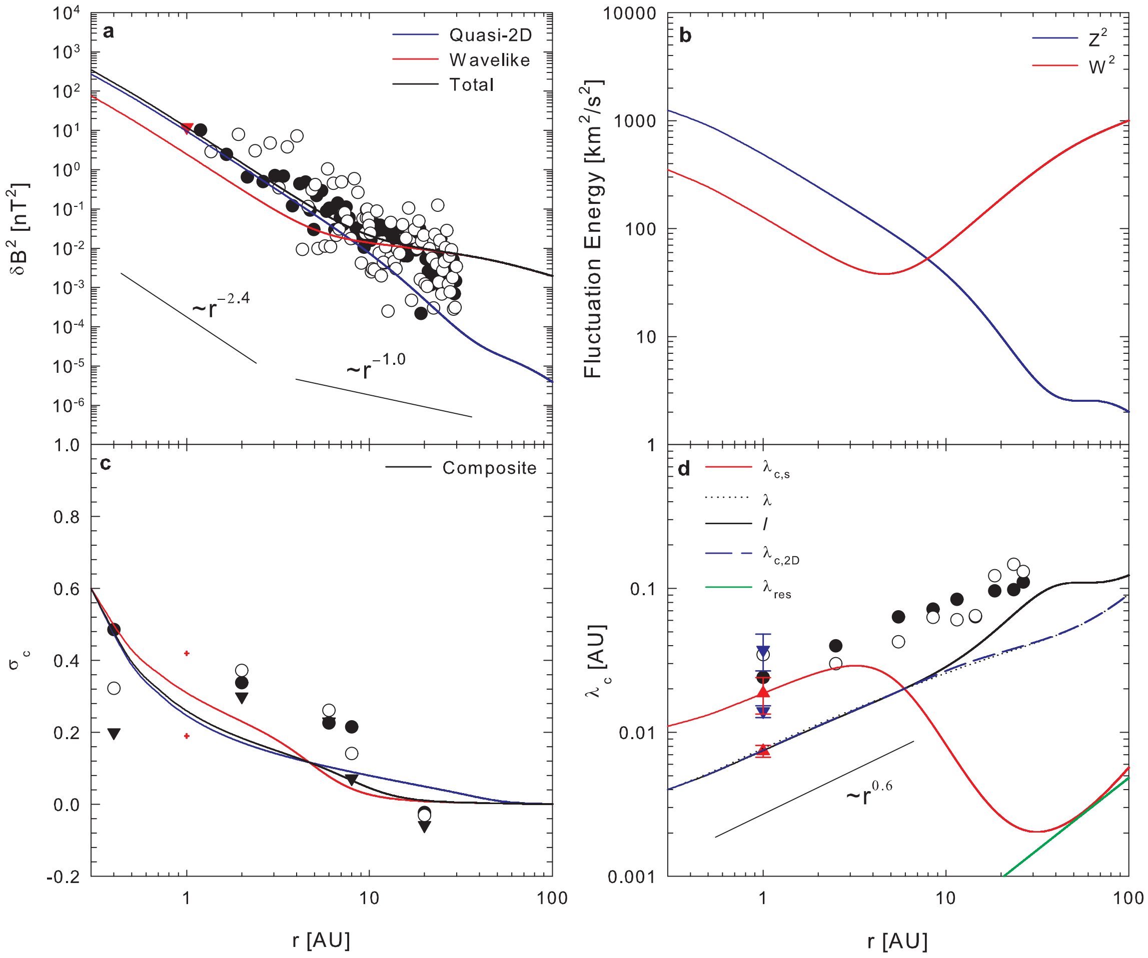

Figure 3.9: Various solutions of the two-component *Oughton et al.* [2011] turbulence transport model, shown for an assumed Parker HMF as functions of radial distance in the solar ecliptic plane. Panel (a) shows the variances associated with the wavelike and quasi-2D components, as well as the total variance, with data from *Zank et al.* [1996], and one point from the results presented by *Smith et al.* [2006b]; panel (b) the corresponding fluctuation energies; panel (c) the normalised cross-helicities corresponding to each component of the model, as well as the composite cross-helicity (black line), with data from *Roberts et al.* [1987a, b] and *Breech et al.* [2005]; and panel (d) the various correlation lengthscales, with observations from *Matthaeus et al.* [1999a], *Smith et al.* [2001], *Weygand et al.* [2009] and *Weygand et al.* [2011]. See text for details as to boundary conditions used, and assumptions made.

3.4.1 Solutions at selected colatitudes

Figure 3.9 shows the various solutions of the *Oughton et al.* [2011] turbulence transport model in the solar ecliptic plane as functions of heliocentric radial distance for a Parker field, utilizing the boundary values listed for this study in Table 3.2. Panels (b) and (a) of this figure show respectively the fluctuation energies, and variances calculated using Eq. 3.7, along with *Voyager* 1 and 2 observations of the total magnetic variance from *Zank et al.* [1996] (see Subsection 2.3.6 for a more detailed discussion thereof). In panel (b), and correspondingly in panel (a), the wavelike fluctuation energy initially decreases steadily as a function of radial distance, beginning to increase substantially only beyond ~ 5 AU. This behaviour is due to the action of the pickup ion energy-injection term $\dot{E}_{PI}$, which steadily becomes more significant relative to the other terms in Eq. 3.5 at radial distances beyond the assumed ionization cavity scale L_{cav}. The pickup ion term is not present in the quasi-2D fluctuation energy equation, and hence this quantity, along with the variance associated with it, monotonically decreases with increasing radial distance. This result is consistent with the theoretical findings of, *e.g.*, *Hunana and Zank* [2010]. It is an interesting consequence of the injection of pickup-ion energy into only one of the components that the slab/2D anisotropy usually observed at Earth [*e.g. Bieber et al.*, 1994] effectively reverses beyond ~ 5 AU, a result also found by *Oughton et al.* [2011].

Initially, the decrease in both the quasi-2D and wavelike fluctuation energies proceeds at the same rate, being driven partly by the mixing and stream-shear terms which are here assumed to be the same for both components. The primary reasons for the decrease of Z^2 are the de Kármán and Howarth-Taylor decay of the Z fluctuations due to interactions with Z fluctuations, and the decay of quasi-2D fluctuations due to interactions with W-type fluctuations. The decay of the wavelike fluctuations in the very inner heliosphere is dominated by the second and third terms of Eq. 3.5, which describe the effects of weak turbulence, and an Iroshnikov-Kraichnan decay of the W fluctuations [*Oughton et al.*, 2011]. It is therefore not surprising that the radial dependence exhibited by the variances associated with both components display a radial dependence of $\sim r^{-2.4}$, in contrast to the WKB-dependence of r^{-3}. The total variance, denoted by the solid black line in panel (a), is calculated as the sum of the quasi-2D and wavelike variances, and follows the trend of the *Zank et al.* [1996] data rather well. Within about 5 AU, the total variance in the ecliptic also exhibits an $\sim r^{-2.4}$ radial dependence. Due to the action of the pickup-ion term on the wavelike component, it subsequently displays a flatter, $\sim r^{-1.0}$ radial dependence at larger radial distances.

The normalised cross-helicities corresponding to the wavelike and quasi-2D fluctuations as well as a composite cross-helicity defined in Eq. 3.18 are shown in panel (c) of Fig. 3.9 with data from *Roberts et al.* [1987a], *Roberts et al.* [1987b] and *Breech et al.* [2005]. All three quantities drop to values very close to zero within ~ 50 AU, but the normalised cross-helicity associated with the quasi-2D fluctuations remains greater than zero for a longer distance than that associated with the wavelike component. This is due to the action of the pickup-ion term, in that the extra fluctuation energy added to the wavelike component acts so as to decrease the normalised cross-helicity associated with it. For the purposes of comparison with data, the composite cross-helicity remains within the range of almost all the data points, excepting the last triad at 20 AU.

The several correlation scales are depicted in panel (d) of Fig. 3.9 along with various observations discussed in detail in Subsection 2.3.5. At 1 AU, both the parallel and perpendicular correlation lengthscales agree well with the observations for these quantities reported by *Weygand et al.* [2011]. The *Voyager* values, reported by *Matthaeus et al.* [1999a] and *Smith et al.* [2001] are, due to the geometry of the heliospheric magnetic field beyond $\sim 2 - 10$ AU, more properly to be compared with the perpendicular scales [*Zank et al.*, 1996; *Oughton et al.*, 2011]. These

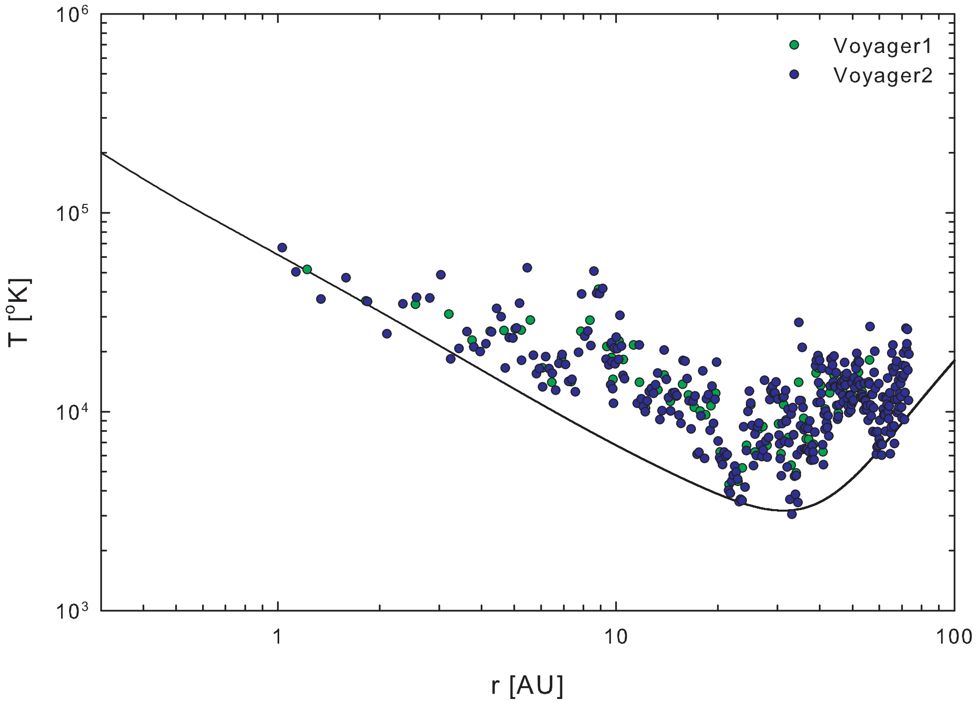

Figure 3.10: Ecliptic solution of the temperature equation (Eq. 3.23) of the two-component *Oughton et al.* [2011] turbulence transport model, with assorted *Voyager* data [*Smith et al.*, 2001].

observations, however, are not sufficient to allow one to distinguish as to whether they pertain to the perpendicular scale corresponding to the wavelike, or the quasi-2D, fluctuating components. Hence these points are here, as in *Oughton et al.* [2011], compared with a center-of-mass style weighted average of the perpendicular lengthscales, calculated according to Eq. 3.13. This quantity appears to follow the radial trend of the data reasonably well, but is too small by a factor of approximately 2. It is worthwhile to note, however, that *Matthaeus et al.* [2005] report an overestimation by a factor of 2-4 of correlation scales observed using single spacecraft data, compared with the observations acquired by utilizing measurements taken by multiple spacecraft.

The monotonically increasing ($\sim r^{0.6}$) perpendicular correlation scales in Fig. 3.9 are consistent with the consistently decaying quasi-2D fluctuation energy illustrated in panel (b) of Fig. 3.9. Similarly, the increase of the parallel lengthscale is consistent with the behaviour of W^2 within the assumed ionization cavity. The action of the pickup-ion term is reflected in the behaviour of the parallel lengthscale in the outer heliosphere, where it displays a marked decrease as function of radial distance. This decrease commences at approximately the same radial distance as the increase noted in the radial profile of the wavelike fluctuation energy. The parallel correlation scale relaxes in the outer heliosphere to the resonant scale λ_{res} (Eq. 3.15), the scale corresponding to the wavenumber at which energy due to the formation of pickup-ions is injected into the wavelike fluctuation spectrum.

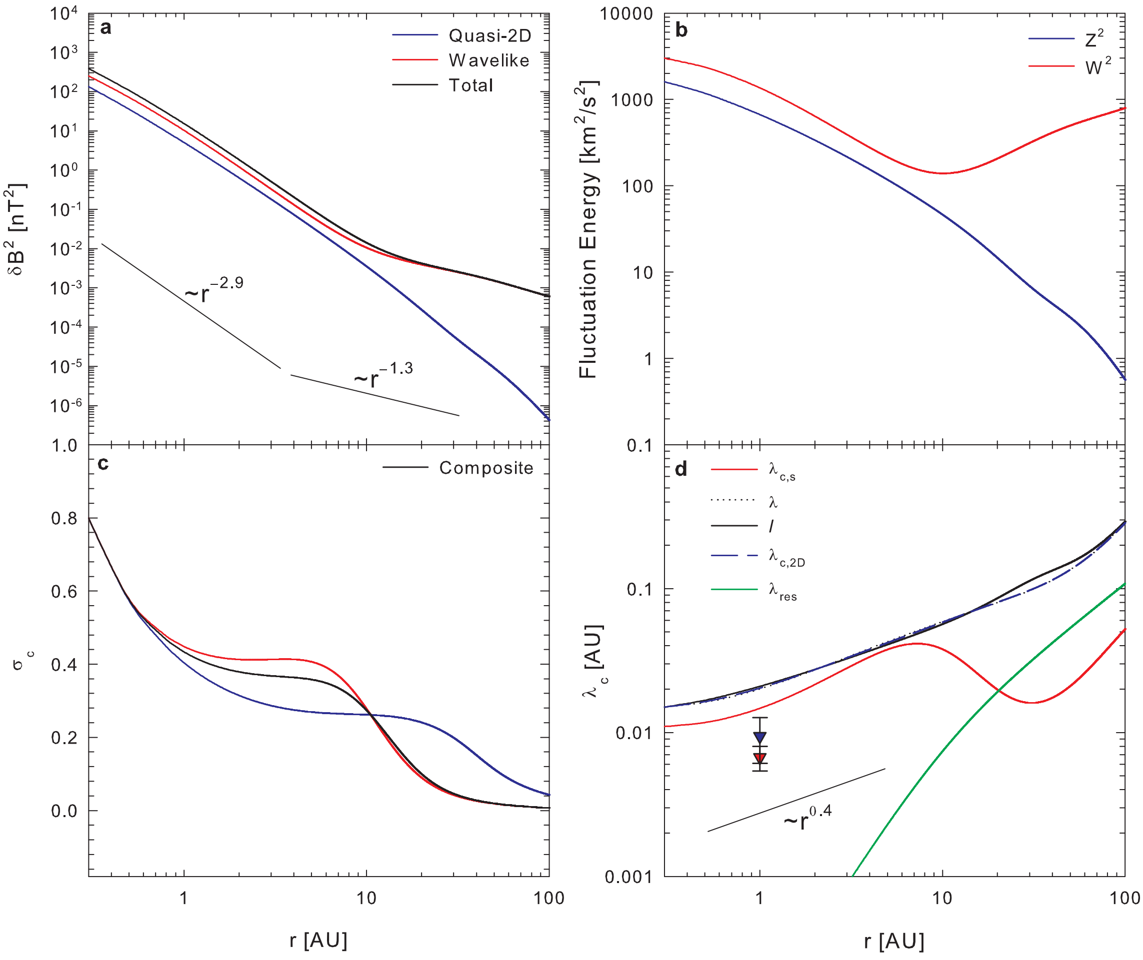

Figure 3.11: Various solutions of the two-component *Oughton et al.* [2011] turbulence transport model for a Parker HMF as functions of radial distance at 10° colatitude. Panel (a) shows the variances associated with the wavelike and quasi-2D components, as well as the total variance; panel (b) the corresponding fluctuation energies; panel (c) the normalised cross-helicities corresponding to each component of the model; and panel (d) the various correlation lengthscales, with some observations reported by *Weygand et al.* [2011]. See text for details as to boundary conditions used and assumptions made. Note that none of the observations reported by *Bavassano et al.* [2000a, b] are here shown as these are more aptly considered along the trajectory of the *Ulysses* spacecraft in Subsection 3.4.3.

Figure 3.10 shows the solar wind proton temperatures yielded by the model as a function of radial distance in the ecliptic plane. Also shown are various *Voyager* data reported by *Smith et al.* [2001] (see Subsection 2.3.7 for a more detailed discussion). The radial profile displayed agrees qualitatively with the data, in that for the inner heliosphere the expected adiabatic profile is reproduced, with a flattening at higher radial distances due to the injection of energy into the wavelike component by the formation of pickup-ions which is modelled to heat the solar wind by means of the turbulent energy cascade. The relatively poor agreement with data, at least in terms of temperature values as opposed to the radial trend at the largest radial distances, is deceptive, as both Voyager spacecraft have at these distances left the ecliptic plane.

In Fig. 3.11 the same format as Fig. 3.9 is used to show the various variances, fluctuation energies, normalised cross-helicities and lengthscales, but at a colatitude of 10°. Note that no *Ulysses* data is included in this figure. Due to the large excursions in latitude of that spacecraft, solutions presented along a radial spoke taken at this colatitude would not reflect the implicit latitudinal dependence of such data. Only the fast solar wind correlation scale observations reported by *Weygand et al.* [2011] are shown, to guide the eye.

Panels (a) and (b) of Fig. 3.11 show respectively the variances and fluctuation energies associated with the wavelike and quasi-2D components of the model. Initially, the variances for both components decrease at the same rate, again partly a consequence of choosing identical turbulence parameters, such as the stream-shear constant, for both components. The rate of decrease of the variances with increasing radial distance, however, is steeper than that seen in the ecliptic solutions, scaling approximately as $r^{-2.9}$. This radial dependence is very close to the $r^{-2.89\pm0.09}$ behaviour reported for the variance in the meridional component of the HMF by *Forsyth et al.* [1996]. Also, if the magnitude of the total variance is considered to be twice that of the variance displayed by the meridional component of the heliospheric magnetic field, the values yielded by the model are quite close to those reported by *Forsyth et al.* [1996].

The radial dependence of Z^2 and W^2 and the variances in the very inner heliosphere, where the pickup-ion term is not yet significant, is dominated by the action of the first three terms in Equations 3.4 and 3.5. At these latitudes the mixing term M is larger, as can be seen in Fig. 3.5, but its increase is somewhat balanced by the lower value assumed here for the stream-shear constant (see Fig. 3.6), such that the radial dependence now resembles the r^{-3} dependence predicted by the WKB theory. Here, as in the ecliptic solutions, there is a marked departure in behaviour between the two components beyond the ionization cavity length scale due to the effect of the increasing pickup-ion term on the wavelike fluctuation energy. The smaller stream-shear constant, as well as the effect of the smaller Alfvén speed on the term modelling the effects of an Iroshnikov-Kraichnan type decay of the wavelike fluctuations in Eq. 3.5, causes the total variance to assume a slightly steeper radial dependence of $\sim r^{-1.3}$ at these latitudes. This happens even though the lower solar wind proton density assumed at these latitudes, along with a solar wind speed that is effectively double that assumed in the ecliptic plane, act so as to increase the value of $\dot{E}_{PI}$.

Panel (c) of Fig. 3.11 illustrates the radial behaviour of the various cross-helicities at 10° colatitude. Here, as in the ecliptic, both the quasi-2D and wavelike normalised cross-helicities decrease fairly steadily with increasing radial distances. Beyond ~ 5 AU, the wavelike normalised cross-helicity goes to values extremely close to zero relatively quickly due to the action of the pickup-ion source term on the wavelike fluctuation energy, as opposed to its quasi-2D analogue which retains a finite value even at 100 AU. The slower decrease of the quasi-2D normalised cross-helicity is consistent with the uniformly steep decrease, and hence lower values at greater radial distances, of Z^2 shown in panel (c).

The various lengthscales yielded by this model are shown in Fig. 3.11 (d). Here as in the ecliptic plane the composite perpendicular lengthscale increases relatively uniformly with increasing

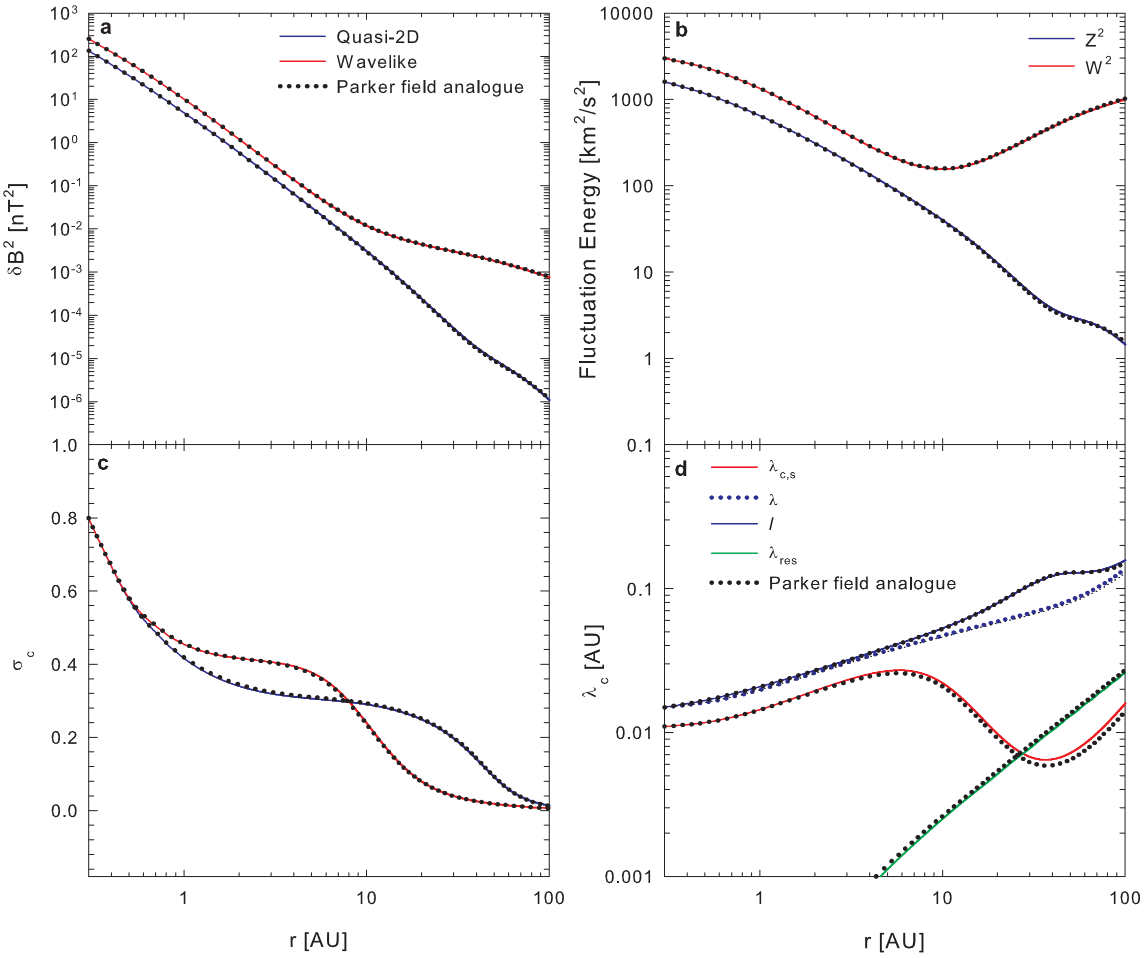

Figure 3.12: Various solutions of the two-component *Oughton et al.* [2011] turbulence transport model for a reduced Schwadron-Parker hybrid field as functions of radial distance. Solutions are taken at 50° colatitude, where the transition function governing the Schwadron-Parker hybrid field assumes a maximum value. Panel (a) shows solutions for the variances associated with the wavelike and quasi-2D components, as well as the total variance; panel (b) solutions for the corresponding fluctuation energies; panel (c) solutions for the normalised cross-helicities for each component of the model; and panel (d) solutions for the various correlation lengthscales. Solutions acquired using a Parker field are also shown, and indicated by means of black dotted lines. Composite quantities shown in previous figures are not included, for the purposes of clarity.

radial distance, displaying an approximately $r^{0.4}$ radial dependence. This is due to the relatively monotonic decrease in Z^2. The parallel lengthscale in the very inner heliosphere mimics to some degree the increase in the perpendicular lengthscales. The ratio of the parallel to composite perpendicular lengthscales is ~ 0.70 at 1 AU, close to the value of 0.71 ± 0.29 reported by *Weygand et al.* [2011]. At larger radial distances the influence of $\dot{E}_{PI}$ is again felt, but the drop-off is not as steep as in the ecliptic, due to the larger values λ_{res} (the green line) assumes at these latitudes. Overall the values assumed by the parallel and perpendicular correlation lengthscales are considerably larger than the *Weygand et al.* [2011] values shown in panel (d). The reason for this, however, is that the boundary values for these quantities were chosen so as to agree with the *Bavassano et al.* [2000a, b] observations along *Ulysses'* trajectory.

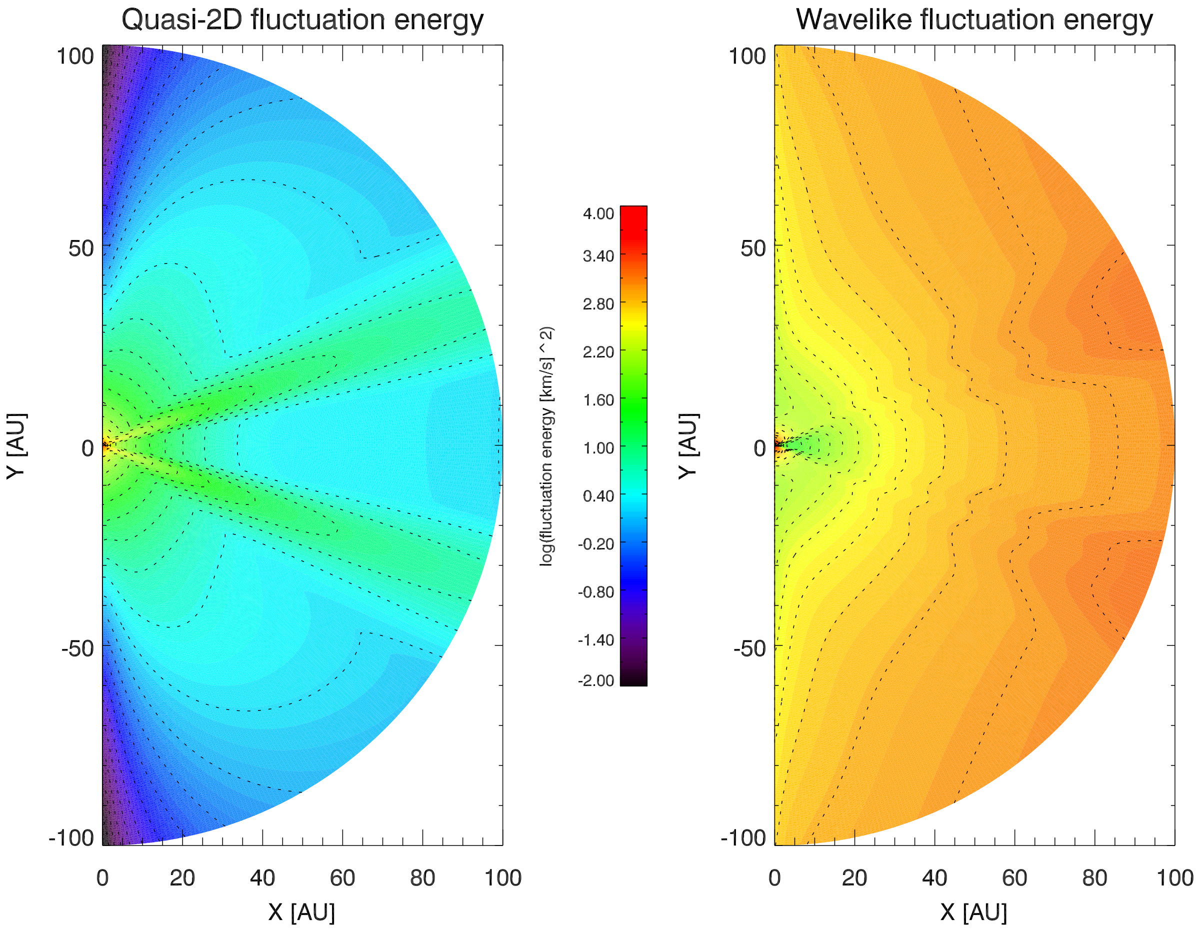

Figure 3.13: Meridional slices, taken at 0° azimuth, of the quasi-2D (left panel) and wavelike (right panel) fluctuation energies. Note that for these solutions a Parker field has been used.

Figure 3.12 follows similarly to Figures 3.9 and 3.11, but the various quantities illustrated are now taken at 50° colatitude for a Schwadron-Parker hybrid field. Results taken for a Parker field at this colatitude are indicated by black dotted lines, to accentuate differences due to the choice of HMF model. Note that composite quantities are not shown in this figure, for the purposes of clarity. This particular colatitude was chosen because the transition function governing the hybrid field assumes its maximum value here (see Fig. 3.3), and therefore any differences in results yielded by the turbulence transport model due to the choice of field model would be maximized. As the values of large-scale fields, the turbulence related inputs, and initial boundary values here used are similar at this latitude to those they assume at 10° colatitude, the discussion above pertaining to the various quantities in Fig. 3.11 applies equally well here. The variances and fluctuation energies for both HMF models, as shown in panels (a) and (b) respectively, are almost identical. The largest deviation between the models for Z^2, and hence its associated variance, amounts to a $\sim 6.3\%$ greater value for the hybrid field. The largest deviation for W^2 amounts to $\sim 2.4\%$. The normalised cross-helicities, shown in panel (c) of the same figure, are almost identical for the two field models, with the greatest percentage deviations for $\tilde{\sigma}_c$ and σ_c being $\sim 1.6\%$ and $\sim 3.3\%$, respectively. When the perpendicular

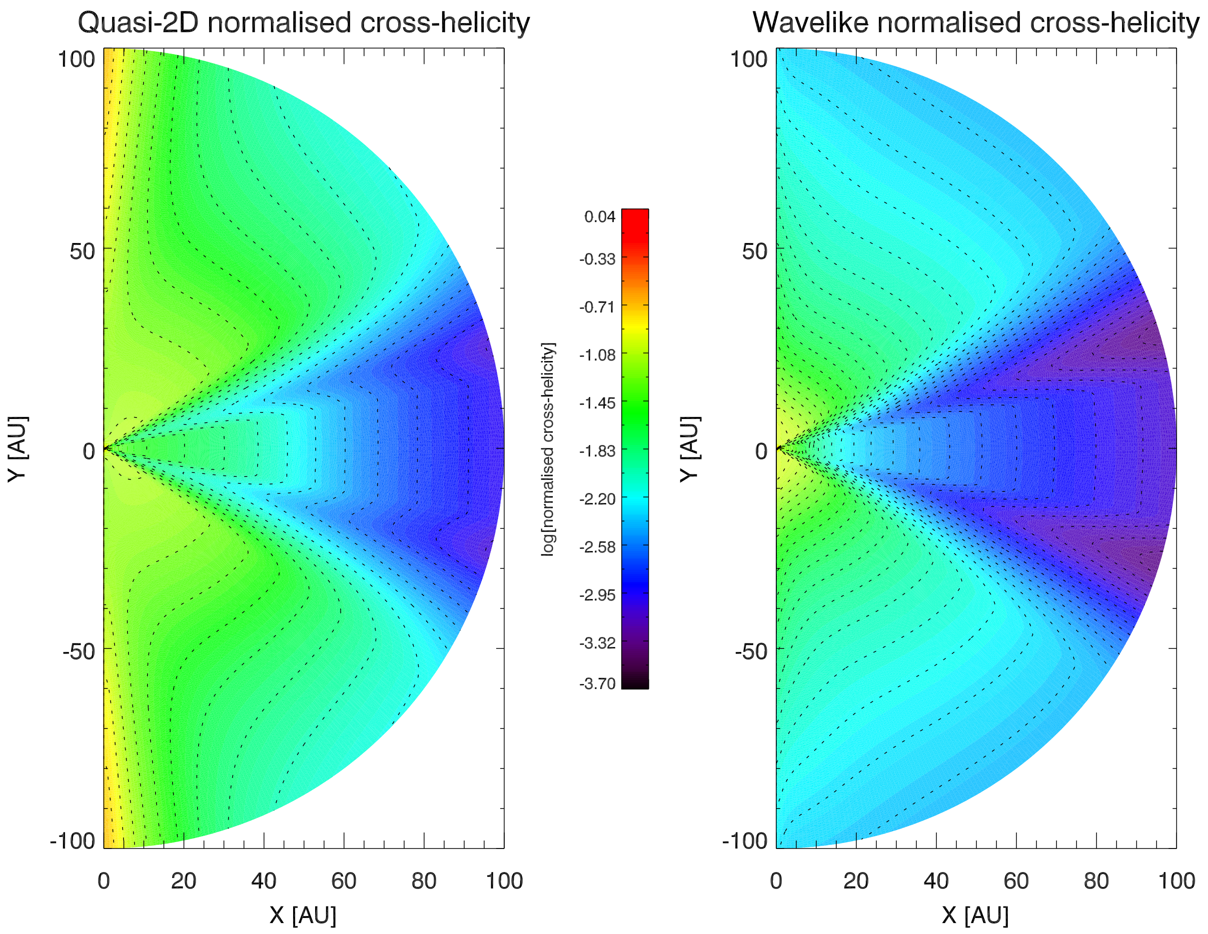

Figure 3.14: Meridional slices, taken at $0°$ azimuth, of the normalised cross-helicities associated with the quasi-2D (left panel) and wavelike (right panel) fluctuation components. Note that for these solutions a Parker field has been used.

correlation lengthscales are considered, the greatest percentage deviation for l is $\sim 3.3\%$, while that for λ is a maximum of $\sim 6.3\%$ due to the Alfvén speed dependence in Eq. 3.12. The largest deviation shown for any of the quantities here considered is that of the parallel correlation scale, which is $\sim 13.5\%$ larger for the Schwadron-Parker field. This is due to its strong dependence on the resonant scale, also shown, which is also affected by the change in HMF model.

The relatively small differences between the two sets of solutions are not unexpected. The reduced transition function employed here to govern the nature of the Schwadron-Parker hybrid field acts so as to rather severely limit differences between the models. Moreover, the inputs to the turbulence transport model have been shown in Subsection 3.3.2 to be relatively insensitive as to the choice between these two HMF models. Therefore, in subsequent chapters of the present study, a single set of boundary values will be employed for modulation studies using either HMF model.

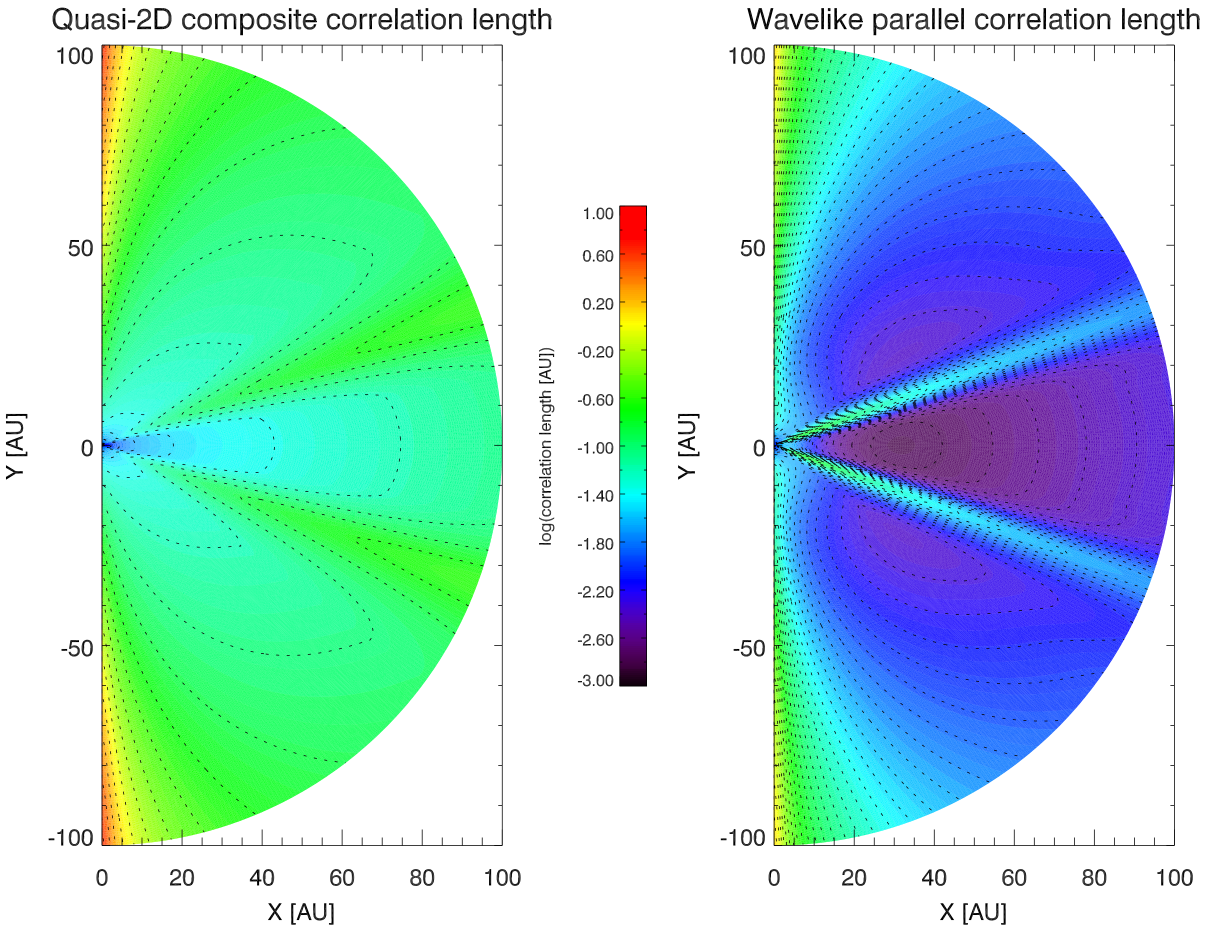

Figure 3.15: Meridional slices, taken at 0° azimuth, of the composite perpendicular correlation lengthscale, defined as in Eq. 3.13 (left panel), and parallel correlation lengthscale (right panel). Note that for these solutions a Parker field has been used.

3.4.2 Global solutions

A more global perspective on the results yielded by the two-component turbulence transport model can be acquired by considering contour plots of the various quantities. Figures 3.13 and 3.15 show the contours of the logarithms of the fluctuation energies Z^2 and W^2, and the correlation scales, both composite perpendicular and parallel, along meridional slices taken at 0° azimuth. Note that the x-axis is in the ecliptic plane, and the y-axis a line going through the poles of a heliocentric spherical coordinate system. Note that not all the quantities yielded by the *Oughton et al.* [2011] model are so considered, but only those as are pertinent to the modelled spectra used in the present study (see Section 2.4 for more detail as to these) to derive diffusion coefficients in the next chapter. Contours of the normalised cross-helicities have, however, also been included in Fig. 3.14, as these quantities provide a useful diagnostic as to the interaction of the various quantities solved for.

A cursory viewing of Figures 3.13, 3.14, and 3.15 reveals that the general behaviour of all the quantities concerned is governed by the solar wind speed profile, in qualitative agreement with the conclusions of *Erdös and Balogh* [2005]. Another latitudinal effect worth noting, especially for the correlation scales and fluctuation energies, is the strong effect of the latitudinal profile chosen for the stream-shear constant. Nowhere is this more pronounced than in the behaviour of Z^2 (Fig. 3.13, left panel). The right panel, which illustrates W^2, shows a broader 'maximum', extending for a few degrees adjacent to the latitude where C_{sh} is largest. This is due to the effects of the added pickup-ion energy, which, along with the additional driving due to shear effects, lead to an overall increase in the wavelike fluctuation energy with radial distance. It should be noted that no radial dependence is here assumed for the stream-shear constant itself. The apparent decrease in its significance for the quasi-2D fluctuations is simply due to the effects of the r^{-1} dependence of the stream-shear terms in Equations 3.4 and 3.5. Throughout most of the heliosphere, the wavelike fluctuation energy is larger than that of the quasi-2D component, a result that could have interesting implications for cosmic-ray transport.

The behaviour of Z^2 and W^2 at the largest radial distances directly over the poles affords an interesting example of the effects the two fluctuation components have upon one another. The quasi-2D fluctuation energy here assumes lower values than anywhere else in the model heliosphere. This is somewhat surprising, as from Fig. 3.5 the geometric mixing term M is at a maximum over the poles, and acts in Eq. 3.4 so as to increase Z^2. But it also acts to increase W^2, along with the usual addition of energy to that component due to pickup ions, which in turn increases the efficacy of the third term of Eq. 3.4. This term governs the decay of quasi-2D fluctuations due to their interactions with wavelike fluctuations, which leads to a decrease in Z^2. An interesting consequence of this can be seen in the left panel of Fig. 3.14, which actually shows an increase in the quasi-2D normalised cross-helicity due to this decrease in Z^2. Whether this behaviour is realistic or not, however, would be extremely difficult to establish observationally. The faster decay discussed in Subsection 3.4.1 of W^2 at higher latitudes and larger radial distances, relative to that displayed in the ecliptic plane, is reflected in a more gradual drop-off of $\tilde{\sigma}_c$ in regions dominated by the fast solar wind, illustrated in the right panel of Fig. 3.14, as opposed to the faster rate of decrease of $\tilde{\sigma}_c$ in the ecliptic plane. The radial decrease of the normalised cross-helicity associated with the quasi-2D fluctuations is less steep than that displayed by its wavelike analogue, due to the lack of pickup-ion driving. The action of the stream-shear constant is apparent in both these figures as a decrease in both these quantities at latitudes where this parameter is large.

Figure 3.15 shows contours for the composite perpendicular correlation lengthscale (left panel) as defined in Eq. 3.13, and the parallel correlation lengthscale $\lambda_{c,s}$, for a meridional slice at 0° azimuth. Both quantities exhibit larger values, at least for intermediate distances, at latitudes where the stream-shear constants applicable to each component assume relatively large values. This is somewhat unexpected, as shear driving would act to reduce these lengthscales. However, the wavelike and quasi-2D fluctuation energies assume high values at these latitudes, hence this behaviour is due to the terms proportional to these quantities to be found in Equations 3.11, 3.12, and 3.14, which act so as to increase these lengthscales. This is in qualitative agreement with the findings of *Breech et al.* [2008] in that for the single component turbulence

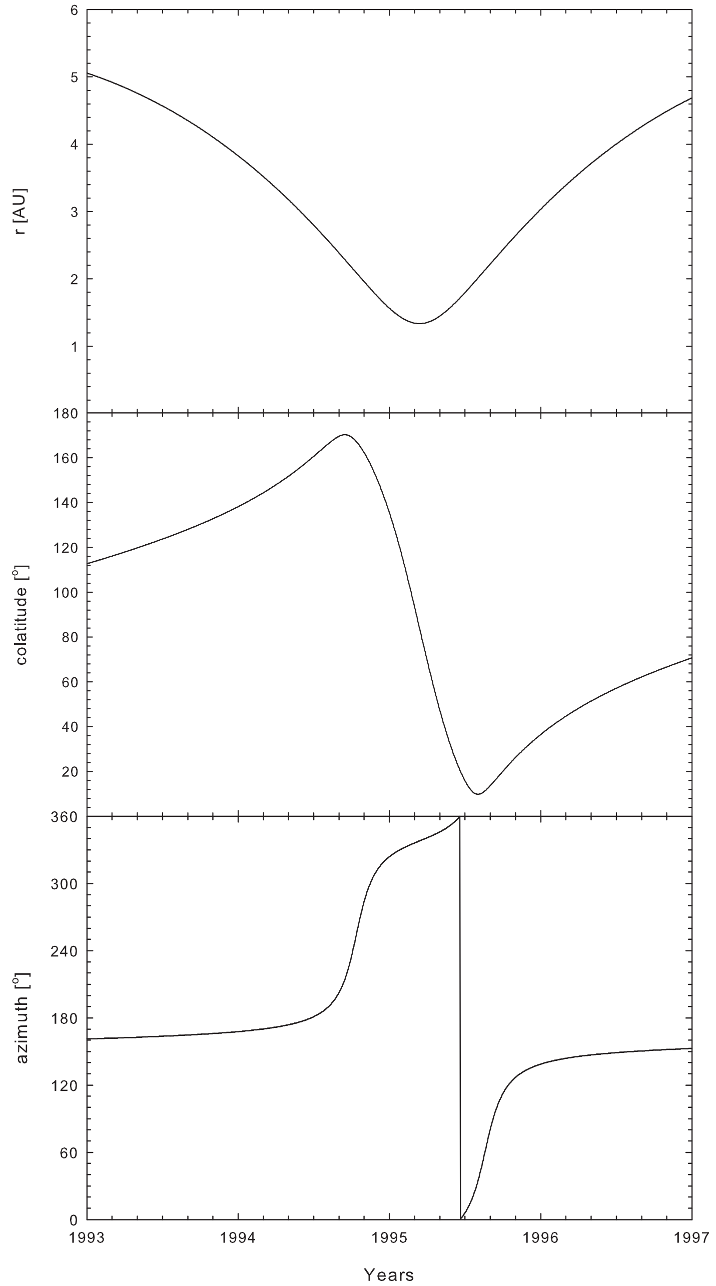

Figure 3.16: Trajectory of the *Ulysses* spacecraft during its first fast latitude scan.

transport model presented in that study, the increased levels of turbulence in regions of greater shear also led to an increased correlation scale. Consequently, in regions of lower shear and hence of less turbulence, both correlation scales here considered show a relative decrease with increasing latitude beyond the regions of high shear, leading to the fleur-de-lis type pattern to be seen in Fig. 3.15. The composite perpendicular scale displays at all latitudes a continuous increase with radial distance, whereas the parallel lengthscale at all latitudes follows the radial behaviour illustrated in Subsection 3.4.1, where after it initially increases, the driving of wavelike fluctuations due to the formation of pickup-ions causes it to start decreasing beyond approximately 5 AU. Beyond about 30 AU it increases again, following the behaviour of λ_{res}. The depth of this initial decrease of $\lambda_{c,s}$ and the distance at which its subsequent increase commences reflect the latitudinal behaviour of λ_{res}.

3.4.3 Solutions along the trajectory of *Ulysses*

The trajectory followed by *Ulysses* was by design highly complicated, with significant excursions in latitude during the fast latitude scans. This can be seen in Fig. 3.16, illustrating the spacecraft's position in terms of heliocentric radial distance, colatitude, and azimuth as a function of time during the first fast latitude scan (FLS). It was during this period that the observations of the fluctuation energy, correlation scale, and normalised cross-helicity reported by *Bavassano et al.* [2000a, b] were made. Note that these data do not include observations taken in the ecliptic plane, leading to a gap spanning about $45°$ in latitude centered on the ecliptic. It is clear that such data cannot be meaningfully compared to the solutions of the *Oughton et al.* [2011] model in the format presented in Subsection 3.4.1, *viz.* with solutions presented along a radial 'spoke' at a fixed colatitude. As noted above, the two-component transport model is here solved for a three-dimensional (r, θ, ϕ) grid. Solution values at gridpoints corresponding to *Ulysses'* trajectory were taken and plotted as a function of time along with the *Bavassano et al.* [2000a, b] data in Figures 3.17 through 3.20. It must be stressed that boundary values were not varied, nor were any parameters or modelled large-scale fields altered in any way so as to create a time-dependence. Rather, the modelled solar minimum conditions were left as is, so as to better simulate prevailing heliospheric conditions during the first FLS. This approach allows for a meaningful comparison between model outputs and spacecraft data, taking into account the complicated implicit spatial dependences of these data. Note that only solutions acquired using a Parker HMF are considered, due to the similarity of these solutions to those for a reduced Schwadron-Parker hybrid field in the inner heliosphere.

Figure 3.17 shows the fluctuation energies corresponding to both the quasi-2D and wavelike components, with their sum. The observations taken by *Bavassano et al.* [2000a, b] are here assumed to pertain to the energy due to all turbulent fluctuations. Therefore, for comparison with the fluctuation energies yielded by the turbulence transport model, the sum of which being proportional to half the total fluctuation energy (see Table 3.1), the values of these data points have been divided by two. Both W^2 and Z^2 increase gradually to peak values in approximately 1995. Shortly thereafter, a significant 'bump' is seen in Z^2 due to the peak in the stream-shear constants at these latitudes. The lack of a significant 'bump' in the wavelike component can be inferred from the global view shown in Fig. 3.13. This gradual increase is due to a combination of the latitudinal excursion of the spacecraft, and the decrease in radial distance to be seen in Fig. 3.16. After 1995, both fluctuation energies exhibit steep drop-offs due to *Ulysses* approaching the ecliptic plane, for which the assumed boundary values for fluctuation energies are much lower. Note that there is a data gap in this region. After a minimum value in the ecliptic, both quantities increase again, more-or-less mirroring the pre-ecliptic be-

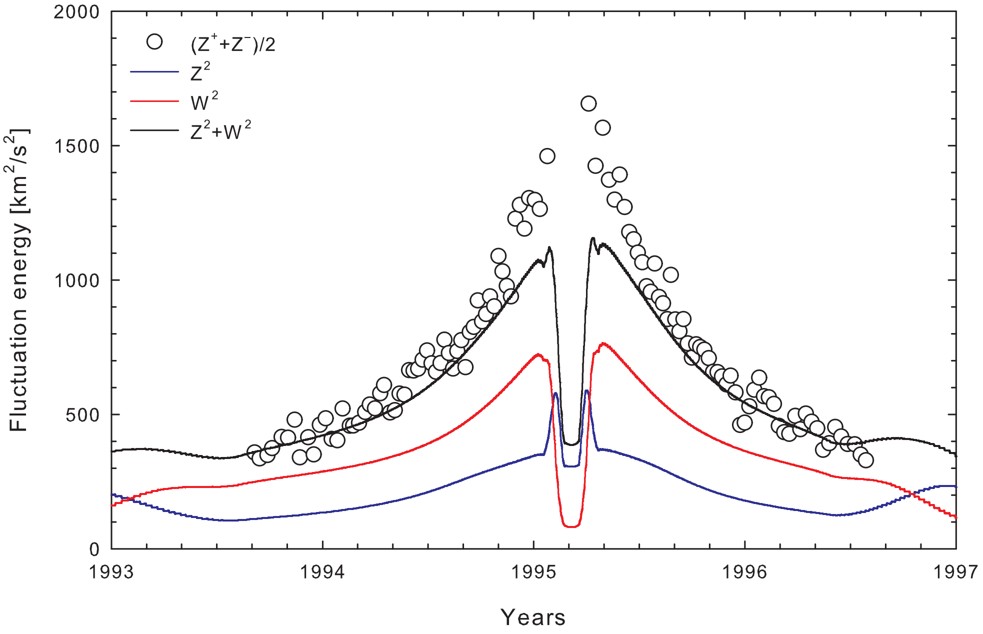

Figure 3.17: Fluctuation energies yielded by the two-component *Oughton et al.* [2011] turbulence transport model along the trajectory of the *Ulysses* spacecraft during its first fast latitude scan. Data shown are from *Bavassano et al.* [2000a, b]. Note the data gap spanning approximately 45° in latitude, centered on the ecliptic plane.

haviour, as *Ulysses* now approaches the 'North' pole. That this mirroring is not exact, is not due to any North-South asymmetries inherent to the model, but rather due to the somewhat asymmetric spacecraft trajectory, most clearly seen in the top panel of Fig. 3.16. The sum of the fluctuation energies behaves similarly to its parts, and initially agrees well with the *Bavassano et al.* [2000a, b] observations. As the spacecraft approaches the ecliptic, however, the model undershoots the data. This is due to the fact that boundary values in the ecliptic were chosen so as to acquire solutions in agreement with ecliptic data, taken using various spacecraft, techniques, and averaging times, which may not be completely comparable to the hourly averaged *Bavassano et al.* [2000a, b] data. It is, however, encouraging that the model agrees reasonably well with most of the observations, along a broad range of the varied spatial positions along the trajectory of *Ulysses*.

The correlation scale observations of *Bavassano et al.* [2000a, b], shown alongside the parallel and composite perpendicular correlation lengthscales yielded by the *Oughton et al.* [2011] model in Fig. 3.18, show a rather broad spread. This, coupled with the fact that it is difficult to say whether one should compare them with a perpendicular or a parallel correlation scale, make it very hard to evaluate model results. Hence the boundary values were here set so as to yield model results that for both lengthscales fall on the lowest values of the data, this being motivated by the reported overestimation of correlation scales acquired from single spacecraft measurements [*Matthaeus et al.*, 2005]. Neither of these lengthscales are incompatible with the

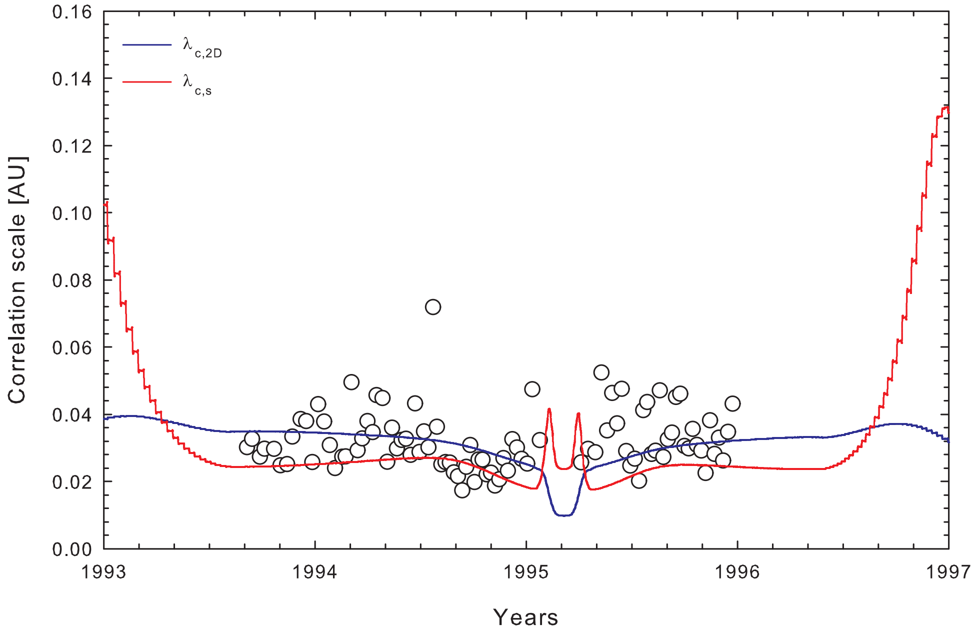

Figure 3.18: Correlation scales, parallel and perpendicular composite, yielded by the two-component *Oughton et al.* [2011] turbulence transport model along the trajectory of the *Ulysses* spacecraft during its first fast latitude scan. Data shown are from *Bavassano et al.* [2000a, b]. Note the data gap spanning approximately $45°$ in latitude, centered on the ecliptic plane.

Bavassano et al. [2000a, b] data. The ratio of the parallel to perpendicular correlation scales remains approximately 0.70 along most of Ulysses' trajectory here considered. This is unsurprising, as at high latitudes, within the radial distances traversed by this spacecraft, both lengthscales yielded by the model have very similar radial dependences (see Fig. 3.11, panel (d), and accompanying discussion). The relatively gradual increase of these quantities with radial distance at high latitudes ($\sim r^{0.4}$ at $10°$ colatitude, for example) leads to the relatively flat pre-1995 model results in Fig. 3.18. Beyond this a sharp 'bump' in the parallel correlation scale corresponding to regions of greater shear can be seen. This sharp increase after 1995, and the lack of it in the perpendicular correlation scale, can again be inferred from the global view, in this case shown in Fig. 3.15. At high latitudes, the composite perpendicular scale is consistently larger than the parallel correlation scale, but this scenario is reversed as model results closer to the ecliptic are considered, consistent with the results shown in panel (d) of Fig. 3.9. The model results beyond the ecliptic again approximately mirror those discussed above.

At higher latitudes and radial distances along *Ulysses'* trajectory, the observations as to the normalised cross-helicity reported by *Bavassano et al.* [2000a, b] show a fairly large spread. The model solutions for the normalised cross-helicities, including the composite value shown in Fig. 3.19 are well within the range of this dataset, at least before 1994.6, and after 1995.5. Agreement, however, again worsens as the spacecraft approaches the ecliptic plane. The modelled normalised cross-helicity associated with the quasi-2D component, as well as that associated

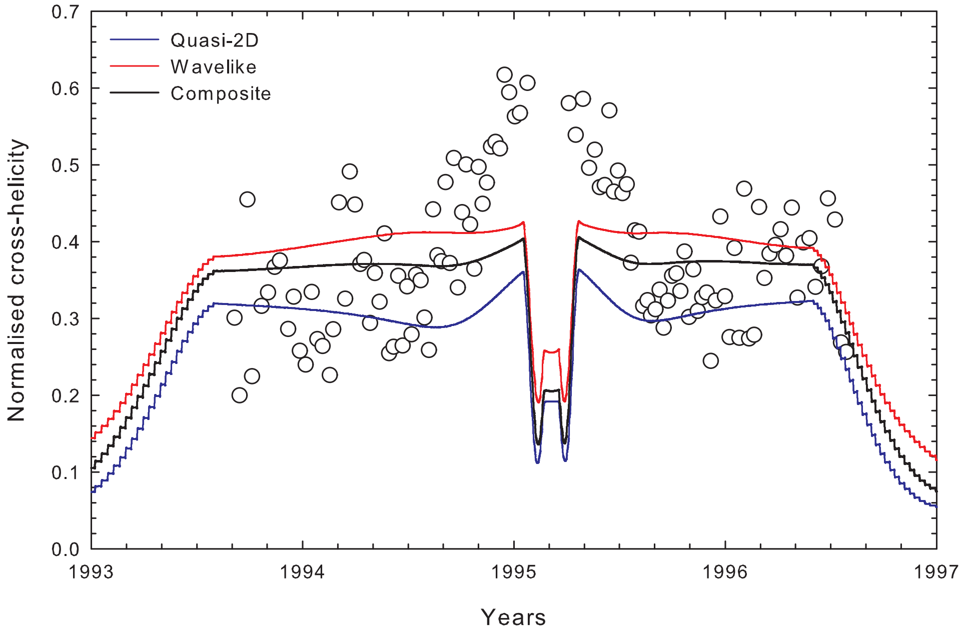

Figure 3.19: Normalised cross-helicities yielded by the two-component *Oughton et al.* [2011] turbulence transport model along the trajectory of the *Ulysses* spacecraft during its first fast latitude scan. Data shown are from *Bavassano et al.* [2000a, b]. Note the data gap spanning approximately $45°$ in latitude, centered on the ecliptic plane.

with the wavelike fluctuating component, exhibit a decrease in magnitude at times associated with regions of increased shear along the spacecraft trajectory, although the values yielded by the two-component model are far below the data at these latitudes. This is partly due to the fact that boundary values for the ecliptic plane were chosen so as to agree with the observational values reported by *Roberts et al.* [1987a, b] and *Breech et al.* [2005]. These ecliptic values were calculated for fluctuation spectra observed over periods of 3, 9, and 27 hours (the *Roberts et al.* [1987a, b] observations) and periods of 12 and 24 hours (the *Breech et al.* [2005] points), the value at each radial distance considered being quite sensitive to this period of observation. The *Bavassano et al.* [2000a, b] normalised cross-helicities were calculated from hourly averaged data, and this difference may contribute to the lack of agreement between model outputs and data near the ecliptic. It may also be due to an inappropriate choice here made of one of the turbulence parameters, such as C_{sh}, significant in the streamer belt.

The last quantity to be considered along the trajectory of the *Ulysses* spacecraft is the solar wind proton temperature, shown in Fig. 3.20. Here the results yielded by the model agree very well with the temperatures observed by *Ulysses* at higher latitudes and radial distances.

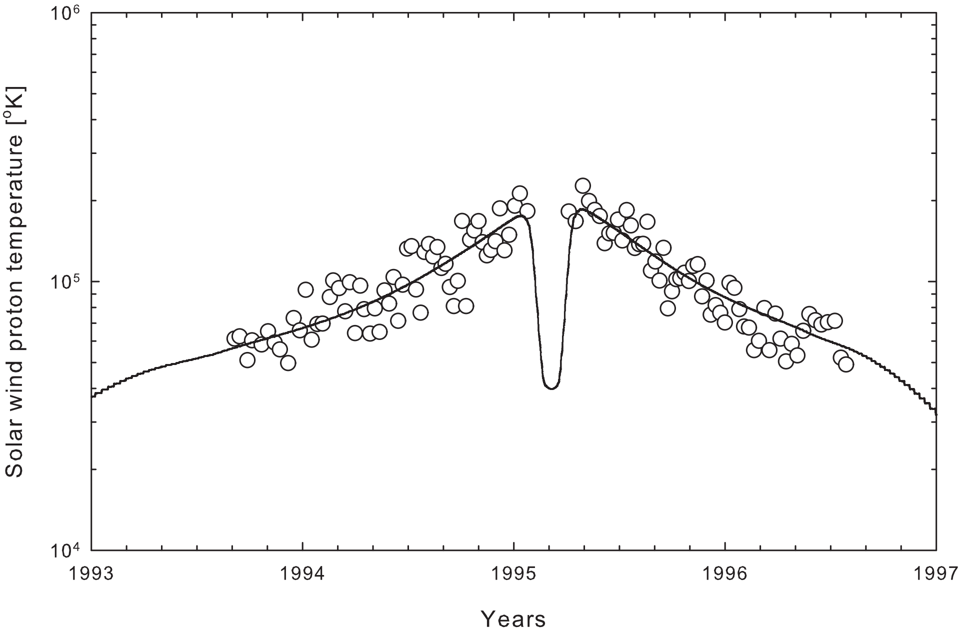

Figure 3.20: Solar wind proton temperatures yielded by the two-component *Oughton et al.* [2011] turbulence transport model along the trajectory of the *Ulysses* spacecraft during its first fast latitude scan. Data shown are from *Bavassano et al.* [2000a, b]. Note the data gap spanning approximately $45°$ in latitude, centered on the ecliptic plane.

3.5 Summary and Conclusions

The two-component turbulence transport model presented by *Oughton et al.* [2011] has been introduced. Choices as to the behaviour of the large-scale fields at solar minimum and turbulence input parameters required by the model have been made, and motivated in the light of observations throughout the heliosphere as well as prior studies conducted with other turbulence transport models. It has been shown that the model can yield results in fair to good agreement with extant turbulence spacecraft data, both in the ecliptic plane and along the trajectory of the *Ulysses* spacecraft. Furthermore, the use of a reduced Schwadron-Parker hybrid field leads to results very similar to those acquired using a purely Parker field. The relatively small effect of the hybrid field on the results of the turbulence transport model implies that a single set of boundary values for the two-component model may be used for both fields, facilitating subsequent modulation studies.

The turbulence quantities yielded by this transport model will in the next chapter be used as inputs to the turbulence power spectra discussed in Section 2.4. Although these spectra require inputs pertaining strictly to the slab/2D turbulence model discussed in the previous chapter, the quasi-2D/wavelike results of the *Oughton et al.* [2011] provide a fair approximation to their 2D/slab analogues [*S. Oughton*, *private communication*, 2011], the set of fluctuations described by the slab/2D model being essentially a subset of that described by the quasi-2D/wavelike model [*Oughton et al.*, 2006]. These spectra will be used in *ab initio* expressions for cosmic-ray mean free paths, whose spatial dependences will now depend on the behaviour of the solutions to the two-component turbulence transport model.